

# Birth Kick Distributions and the Spin-Kick Correlation of Young Pulsars

C.-Y. Ng<sup>1</sup> & Roger W. Romani<sup>1</sup>

ncy@astro.stanford.edu, rwr@astro.stanford.edu

## ABSTRACT

Evidence from pulsar wind nebula symmetry axes and radio polarization observations suggests that pulsar motions correlate with the spin directions. We assemble this evidence for young isolated pulsars and show how it can be used to quantitatively constrain birth kick scenarios. We illustrate by computing several plausible, but idealized, models where the momentum thrust is proportional to the neutrino cooling luminosity of the proto-neutron star. Our kick simulations include the effects of pulsar acceleration and spin-up and our maximum likelihood comparison with the data constrains the model parameters. The fit to the pulsar spin and velocity measurements suggests that: *i*) the anisotropic momentum required amounts to  $\sim 10\%$  of the neutrino flux, *ii*) while a pre-kick spin of the star is required, the preferred magnitude is small  $10 - 20 \text{ rad s}^{-1}$ , so that for the best-fit models *iii*) the bulk of the spin is kick-induced with  $\bar{\Omega} \sim 120 \text{ rad s}^{-1}$  and *iv*) the models suggest that the anisotropy emerges on a timescale  $\tau \sim 1 - 3\text{s}$ .

*Subject headings:* pulsars: general — stars: rotation – supernovae

## 1. Introduction

The high velocity of pulsars, at least an order of magnitude larger than their parent population (Hobbs et al. 2005), has been a long standing puzzle. Of the many models proposed, all except the classic Blaauw (1961) binary break-up mechanism rely directly or indirectly on the large release of gravitational binding energy associated with the core collapse event. Since the fastest observed pulsars have  $v > 10^3 \text{ km s}^{-1}$  (Cordes, Romani, & Lundgren 1993; Chatterjee et al. 2005), i.e. bulk velocities  $> 3 \times 10^{-4} c$ , binary break-up is clearly inadequate and a viable mechanism must tap an appreciable fraction of the collapse momentum. However, a wide range of physical processes can still be invoked (e.g. Lai, Chernoff, & Cordes

---

<sup>1</sup>Department of Physics, Stanford University, Stanford, CA 94305

2001; Janka et al. 2005), so gross energetic constraints alone do not solve the pulsar kick problem.

Recent progress has come from studies that probe the *vector* nature of the kick. For example Fryer & Kusenko (2006) argue that neutrino-driven kicks (which may even be crucial for successful explosion) will produce fast supernova remnant (SNR) velocities along the pulsar velocity vector, while ejecta-driven (recoil) kicks should have fast ejecta opposite to the pulsar motion. The pulsar itself also contains kinematic evidence of the kick geometry, since both the velocity and spin directions are in principle measurable. These linear and angular momenta are fossils of the core collapse which can remain inviolate for as much as  $10^6$  yr before acceleration in the Galactic potential perturbs the velocity or torques perturb the spin. Thus mechanisms that are spin-dependent can leave a fossil record in the kick distribution (Lai et al. 2001; Romani 2005). Conversely, kicks can leave a record in the spin distribution (Spruit & Phinney 1998).

The key to making such tests is accurate measurement of pulsar motions and pulsar spins. For the former, the most important progress has been the dramatic improvement in the quality and quantity of VLBI astrometric proper motions (Chatterjee et al. 2005). This work makes it possible to have a vector proper motion (and in a number of cases a parallax, and hence a 2-D space velocity) for most moderately bright,  $\geq$  few mJy, pulsars within 2-3 kpc. An even larger sample of approximate proper motions has been obtained from refined analysis of long term timing records (Hobbs et al. 2005). Together these methods provide useful space velocities for several dozen young pulsars within 3 kpc. Association with parent supernova remnants can provide a few additional proper motion estimates for interesting pulsars at larger distances.

More difficult to measure is the spin direction. The classic approach is to adopt the ‘rotating vector’ (RV) model for pulsar polarization and assign the projected position angle (PA) of the spin axis to the absolute (Faraday ‘rotation measure’ RM corrected) position angle of the polarization at the phase of maximum PA sweep. This method suffers major systematic uncertainties due to poor matches to the expected RV model sweep as well as an intrinsic  $\pi/2$  ambiguity according to whether the emission is in the normal or orthogonal mode; early analyses (Deshpande, Ramachandran, & Radhakrishnan 1999) were not at all conclusive. However, recent improved polarization measurements and RM corrections have provided convincing statistical evidence for a projected 2-D correlation between the directions of polarization PA and the proper motion (Johnston et al. 2005; Wang, Lai, & Han 2006a). Even better, in several cases excellent *CXO* images have made it possible to measure accurately the pulsar spin position angle and its inclination from the plane of the sky using the symmetry axis of the surrounding pulsar wind nebula (PWN) (Ng & Romani 2004). Fi-

nally, in a few cases, one can also independently estimate the original post-supernova spin of the pulsar. With the 3-D spin orientation and amplitude, comparison with the projected 2-D motion allows even more powerful tests of the nature of the birth kick.

In this paper we explore the possibility of comparing the new vector data on pulsar spins and speeds with the dynamics of core collapse. The structure of the paper is as follows. In section §2.1, we describe three simple models of the luminosity and size evolution of a proto-neutron star, which we will follow in estimating the effects of a birth kick. In section §2.2, we summarize the effect of momentum deposition on kick and spin (following Spruit & Phinney 1998) and show how the integrated kick controls the birth properties of the pulsar. We also comment on the results of Wang, Lai, & Han (2006b), whose related but somewhat simpler study of kick evolution appeared while we were writing up this paper. In Section §3, we discuss the sample of nearby and/or young pulsars that we will use for comparison with the models, emphasizing the important objects for which we have more complete knowledge of the post-kick state of the star. Section §4 describes a population simulation that allows us to compare the *distribution* of birth properties with the observed neutron stars for the several models. Section §5 summarizes the fit results that constrain the basic parameters in the kick models. We conclude by discussing the status of the spin-kick comparison, the insight that the present data give us into the physics of the pulsar kick, and the prospects for further refinement of these tests.

## 2. Core-Collapse Luminosity-Driven Kicks

In this study, we consider some simple models for a kick associated with the large luminosity of the post-bounce proto-neutron star. Our assumptions are: *i*) that the asymmetric momentum (kick) scales roughly as the emergent neutrino luminosity, possibly with a delayed onset; *ii*) that the *net* thrust originates from a region fixed with respect to the star; and *iii*) that the thrust may be at a finite angle to the local normal. Of course, this net thrust may simply be the surface average of a complex distribution of local forces. However, we assume that the sum of these has a stable component with respect to the star on the timescale of the initial rotation and cooling. If the thrusts are impulsive and random then, as argued by Spruit & Phinney (1998) and illustrated numerically by Wang et al. (2006b), the final velocity and spin tend to become randomly oriented. Note also, as discussed by Spruit & Phinney (1998), that if there is no initial rotation, the result of a single kick is an orthogonal spin; we will show that the preferred models have a small initial rotation, but the bulk of the spin is introduced by the kick itself.

The simplest realization of this picture would be asymmetric neutrino emission mediated

by strong  $B$ -fields. Arras & Lai (1999a,b) suggest that due to weak interaction parity non-conservation, the neutrino emission depends on the magnetic field, both through simple field-dependent opacities and through helicity-sensitive scattering in the presence of a strong field. They suggest that the total asymmetry in the neutrino flux is  $\sim 0.1B_{15}\bar{E}_\nu^{-2} + 0.002B_{15}/T$  where  $B = 10^{15}B_{15}$  G is the magnetic field strength,  $\bar{E}_\nu$  is the mean neutrino energy in MeV and  $T$  is the temperature in MeV. Clearly, very large fields are needed to produce a significant net kick. However, this model does provide a natural ‘anchor point’ on the star and, through the field angle at the surface, a plausible mechanism for non-normal kicks.

Other possibilities also exist. For example, the net momentum might be generated by asymmetric neutrino coupling to matter in the envelope (Socrates et al. 2005), or by ‘neutrino star-spots’ induced by the magnetic field (Thompson & Duncan 1993), or even by hydrodynamic motions associated with accretion onto the neutron star (e.g. Blondin & Mezzacappa 2006). In the last case, fall-back instabilities may apparently build to large amplitude. Scheck et al. (2006) have presented a detailed set of 2-D hydrodynamic simulations suggesting that large recoil velocities of neutron stars occur naturally when  $m = 1$  instabilities with strong narrow down-flows develop. Here the kick velocity is dominated by the gravitational attraction of the dense down-flow. (A neutrino hot spot associated with this flow does in fact generate anisotropic emission, but its kick, a  $\sim 10\%$  correction, is opposite that of the gravitational term). Our model does not, of course, capture the full dynamical content of such hydrodynamical kicks, and certainly the neutrino light curve does not fully describe the thrust. However this luminosity profile does provide a characteristic duration for energetic processes associated with the core collapse. The physical interpretation is thus not as clear as for the direct neutrino kick scenario, but the characteristic energetics and time scale modeled in our fits can still probe the underlying physics.

## 2.1. Proto-Neutron Star Luminosity Models

We first start from a simple cooling model, where the neutron star is optically thick to neutrinos and the hot envelope is a dominant contribution to the moment of inertia. If the star’s gravitational binding energy is promptly released and lost as neutrino radiation from the surface of the proto-neutron star, then the proto-neutron star is in thermal equilibrium and the evolution of its radius  $R_{NS}$  is ‘*quasi-stationary*’ and determined by the conservation of energy:

$$L_\nu(t) \sim \frac{d}{dt} \frac{GM^2}{R_{NS}} .$$

We show here results using the neutrino luminosity  $L_\nu$  from Fig. 3 in Burrows, Klein, & Gandhi (1992) but have tried different  $L_\nu(t)$  from the literature. The results are quite insensitive to

the details of any standard cooling curve. In the simulation, the initial proto-neutron star radius is set to a generic value of 100 km. As shown in Fig. 1, a final radius of 14.7 km is obtained, which is determined by the total neutrino fluence.

At the opposite extreme, we can assume that both the envelope and core are highly degenerate at bounce (for reviews: Janka et al. 2004; Kotake, Sato, & Takahashi 2006). In this case,  $R_{NS}$  is independent of  $L_\nu(t)$  and the kick essentially acts at a constant radius throughout the cooling. We call this extreme the ‘*static*’ model. In our simulations we take this as  $R_{NS}=10$  km, constant throughout the kick.

Results from more physical numerical simulations suggest real neutron star behavior is between the two limiting cases above. To illustrate this, we examined the results of 2-D hydrodynamic simulations from Rampp & Janka (2002) and Janka et al. (2004). These authors employ a Multi-Dimensional Boltzmann Transport and Hydrodynamics (MDBTH) code to follow the neutrino advection and diffusion. In Fig. 2 we reproduce the mass shell trajectories and show the  $\nu_e$  photosphere as it evolves during the initial cooling. As one sees, the neutron star initially has a large but optically thin envelope. We will assume the thrust is imparted near the neutrinosphere, but the whole star is forced to co-rotate. The time varying moment of inertia can be followed by integrating across these shells. The simulations using this evolution are referred to as ‘ *$\nu$ -transport*’ models. Fig. 1 compares the basic behavior for the models showing  $L_\nu(t)$  and the effective  $R_{NS}(t)$ . The ‘*static*’ model has, by assumption the same neutrino light curve as the ‘*quasi-stationary*’ picture, albeit at fixed  $R_{NS}$ . In the case of the ‘ *$\nu$ -transport*’ model, the simulations available stopped at  $t = 0.46$  s (marked). We extrapolate with simple matched exponentials to take the curves to 50 s.

## 2.2. Kick Dynamics

We wish to model a (possibly non-normal) net thrust at a fixed point  $\vec{r}$  on the proto-neutron star surface which scales with the  $L_\nu(t)$  multiplied by a constant asymmetry  $\eta$ . The thrust is given by

$$F_\nu(t) \sim \eta \frac{L_\nu}{c} .$$

The angular momentum  $\vec{J} = I\vec{\Omega}$  evolves according to

$$\vec{J} = \int \vec{r} \times \vec{F}_\nu dt + I_i \vec{\Omega}_i ,$$

where  $I_i$  and  $\vec{\Omega}_i$  are the initial moment of inertia and angular velocity before the kick respectively. Similarly, the linear momentum is determined by

$$\vec{p} = \int \vec{F}_\nu dt .$$

As we are modeling isolated young neutron stars, three angles determine the kick geometry as illustrated in Fig. 3:  $\alpha$  is the polar angle of the kick position,  $\theta$  is the off-axis angle of the kick from the surface normal, and  $\phi$  is the azimuth angle of the kick about the normal, with  $\phi = 0$  closest to the initial spin axis. Note that we are ignoring any initial space velocity of the progenitor, since with typical values of only a few  $\text{km s}^{-1}$ , it is negligible compared to the kick velocity of several hundred  $\text{km s}^{-1}$ . However, some modest fraction of presently isolated young neutron stars are released from the break-up of pre-existing binaries (Dewey & Cordes 1987; Tauris & Takens 1998; Fryer, Burrows, & Benz 1998). In this case, these may have an initial velocity of as much as  $100 \text{ km s}^{-1}$  (the Blaauw mechanism). If there is no relation between this initial velocity and the initial spin, then this pre-natal velocity may be added to the post-kick speed in quadrature. The main effect is to blur the correlations described below. If, however, there is a fixed relation between the orbital speed and the pre-kick spin or the kick itself, then this fourth angle must be introduced to the geometry. As these cases represent a small fraction of the single neutron star population, we ignore them here; however such considerations may be important to descriptions of kicks for neutron stars presently found in binaries. We defer discussion of such models to a future communication.

During the kick, directions of  $\vec{r}$  and  $\vec{F}_\nu$  evolve according to the rotation

$$\hat{r}' = \mathcal{R}\hat{r}$$

$$\hat{F}'_\nu = \mathcal{R}\hat{F}_\nu$$

where the rotation matrix  $\mathcal{R}$  is given by

$$\mathcal{R} = \begin{pmatrix} \Omega_x^2 + (1 - \Omega_x^2) \cos \delta & \Omega_x \Omega_y (1 - \cos \delta) - \Omega_z \sin \delta & \Omega_x \Omega_z (1 - \cos \delta) - \Omega_y \sin \delta \\ \Omega_x \Omega_y (1 - \cos \delta) - \Omega_z \sin \delta & \Omega_y^2 + (1 - \Omega_y^2) \cos \delta & \Omega_y \Omega_z (1 - \cos \delta) + \Omega_x \sin \delta \\ \Omega_x \Omega_z (1 - \cos \delta) - \Omega_y \sin \delta & \Omega_y \Omega_z (1 - \cos \delta) + \Omega_x \sin \delta & \Omega_z^2 + (1 - \Omega_z^2) \cos \delta \end{pmatrix} ,$$

$\vec{\Omega} = \Omega \hat{\Omega} = \Omega(\Omega_x, \Omega_y, \Omega_z)$  is the angular velocity and  $\delta = \Omega \Delta t$  is the angle that the star rotates in time  $\Delta t$ .

Given a set of initial conditions, the above equations can be integrated numerically to obtain the kick velocity, initial spin period and alignment angle. Note that in this paper, we call the initial pulsar spin period  $P_0$  which is the value right after the kick. The pre-kick spin is denoted by  $P_i$  ( $\Omega_i$ ), which is a specified parameter of the model.

Fig. 4 shows two example integrations with identical initial parameters except for the pre-kick angular velocities  $\Omega_i$ . The kick is against the initial spin with a component along the surface, thus the angular velocity decreases. However, with  $\Omega_i = 30 \text{ rad s}^{-1}$ , the right panel shows that the torque from the kick is large enough to perturb the spin axis to a new direction, where the kick is more effective in spinning up the proto-neutron star. Note that the initially fast spinner ends up nearly aligned, while the slow spinner is closer to orthogonal. Thus, even though the post-kick spin periods  $P_0$  are quite similar in the two models, information about the pre-kick spin is encoded in the vector direction of  $\vec{\Omega}_0$ . In practice, the typical direction and degree of alignment also depends on the thrust orientation and duration; we show below that comparison with multiple observables can separately probe these various effects.

### 3. Pulsar Sample

Linear and angular momenta are relics of neutron star birth and, if well preserved, can provide important probes of the core collapse physics. Given their vector nature, the alignment angle between them is an important observable. As discussed above, this is particularly sensitive to the kick timescale and geometry and can thus give unique information on the kick dynamics. While objects with measurements of all three observables (velocity  $v$ , initial spin period  $P_0$  and alignment angle  $\vartheta_{\Omega.v}$ ) are rare, the correlations between these are particularly powerful at testing the models.

Only recently have improved pulsar observations made such comparison possible. For example, VLBI astrometry provides unprecedentedly high precision proper motion measurement (e.g. Brisken et al. 2002; Chatterjee et al. 2005). Also, pulsar timing observations (Hobbs et al. 2004; Zou et al. 2005) have recently provided additional (albeit often more uncertain) proper motion values. Altogether these provide several dozens of useful proper motion measurements. For pulsar spins, the direction of the projected spin on the sky plane has been inferred from the radio polarization profile by adopting the rotating vector model, although uncertainty in the emission mode leads to an inherent  $\pi/2$  ambiguity. Recently, Johnston et al. (2005) obtain the spin orientations of 25 pulsars from radio polarization observations and noted significant alignment with the pulsar velocities. Wang et al. (2006a) reanalyze archival polarization data and arrive at similar conclusions. Next, the discovery of X-ray jets and torus structure in PWNe provides an even more powerful (and largely model-independent) way to obtain the pulsar spin orientation for a modest number of objects. Ng & Romani (2004) developed a method of pulsar wind torus fitting to measure the 3-D (not projected!) orientation of the spin axis. So for the vector (2-D) speeds and spin

orientation, progress has been good. In contrast, pulsar initial spin periods remain very difficult to estimate. Currently, only a handful of pulsars have initial spin period estimates (e.g. Table 7 in Faucher-Giguère & Kaspi 2006). As it happens, most of these have PWN structure indicating their spin orientations, but many do not have a precise proper motion measurement. In some cases, we can make an estimate of the space velocity from the structure of the associated SNR, but we must be cautious in applying such model-dependent values.

To select a sample of pulsars with 2-D velocities, we start from the list of pulsar proper motions from Hobbs et al. (2005), selecting young isolated pulsars with  $> 2\sigma$  proper motion measurements. A few objects are added or updated with new measurements (e.g. Chatterjee et al. 2005; Zou et al. 2005; Ng & Romani 2006). Galactic acceleration can affect the trajectories of old pulsars, so we restrict our sample to  $\tau < 5$  Myr (we also have included the interesting pulsar PSR B1133+16, which at  $\tau = 5.04$  Myr is just above this limit). Also, differential Galactic rotation can add appreciably to the observed space velocity of distant pulsars. When the precise distance is unknown, this can cause large errors in reducing the speed and position angle to the local standard of rest. Accordingly, we restrict our sample to  $d < 3$  kpc for pulsars with velocities from astrometric or timing analysis. Table 1 lists the pulsar samples used in this study. The first group of 20 objects have only transverse velocity measurements, hence they are called ‘1-D pulsars’. The next group, referred to as ‘2-D pulsars’, have both a velocity and a projected spin alignment angle. For IC 443 and PSR B1800–21 the spin orientations are obtained from X-ray PWNe, all other 14 spin measurements are from radio polarization observations (Johnston et al. 2005; Wang et al. 2006a). As noted, the proper motions, must be corrected to the birth local rest frame for comparison with the spin directions, as this may affect the position angle by several degrees. Finally, the last group consists of 9 ‘3-D pulsars’ which have estimates in all 3 observables, namely the velocities, initial spin periods and alignment angles, thus allowing for a full vector comparison. These pulsars place the strongest constraints on the model parameters.

We have checked the consistency of the three subsets of pulsars, comparing their velocity and alignment angle distributions with the Kolmogorov-Smirnov (K-S) test. The K-S statistics indicates a probability of 0.34 that the velocities of the ‘1-D’ and ‘2-D pulsars’ are drawn from the same distribution. Comparison of the ‘3-D’ samples with the summed ‘1-D’ and ‘2-D’ ones gives a similar value of 0.33. For the alignment angle, the probability of having the same distribution for the ‘2-D’ and ‘3-D’ pulsars is 0.48. Since the samples are relatively small, these tests are not very stringent but at least there is no evidence that the different measurement methods introduce significant biases in to the sample properties.

We next summarize the status of the several of the particularly interesting ‘3-D pulsars’.



*Crab Pulsar (PSR B0531+21)* Ng & Romani (2006) have measured the pulsar’s proper motion with HST astrometry and compared with the spin vector, which was obtained from pulsar wind torus fitting (Ng & Romani 2004). The initial spin period is derived from the historical age, measured braking index and spin parameters (Manchester & Taylor 1977).

*Vela Pulsar (PSR B0833–45)* Tracing back the motions of dense supernova ejecta knots, Aschenbach, Egger, & Trümper (1995) inferred a supernova explosion site  $14'.9 \pm 7'.2$  away from the pulsar’s current position. With the updated pulsar proper motion from Dodson et al. (2003), the kinematic age of the system is then  $\tau = 20 \pm 10$  kyr. Using the measured braking index of  $n = 1.4 \pm 0.2$  (Lyne et al. 1996), an initial spin period of  $30 \pm 20$  ms is estimated. PA of the pulsar spin axis is obtained by torus fitting (Ng & Romani 2004).

*PSR B0540–69* Based on the estimated pulsar age from the SNR expansion velocity (Reynolds 1985), Manchester et al. (1993) suggest an initial spin period of 38.7 ms. The velocity of the pulsar has an initial estimate by Serafimovich et al. (2004) using HST/WFPC2 images. For the pulsar spin, Ng & Romani (2007, in preparation) fit the X-ray pulsar wind torus to obtain its orientation.

*PSR J0538+2817* Ng et al. (2007) report a VLBA astrometric measurement of the pulsar proper motion. They also discovered symmetric structure around the source in the X-ray observation, which, if interpreted as polar jets or pulsar wind torus, indicates the spin axis. From the offset of the pulsar position with respect to the SNR geometrical center, Romani & Ng (2003) argued for a long initial spin period, which was confirmed by Kramer et al. (2003) with the timing proper motion results and strengthened by the precise VLBA proper motion measurement (Ng et al. 2007).

*PSR B1951+32* The pulsar proper motion is determined by VLBA astrometry (Migliazzo et al. 2002). Assuming the pulsar was born at the center of the shell CTB 80, the authors deduced the pulsar age and its initial spin period. Hester (2000) argue that the  $H\alpha$  lobes observed in the HST image correspond to pulsar polar jets, which indicates its spin orientation. Radio polarization measurements could provide a valuable test of this hypothesis.

*PSR J0537–6910* The X-ray PWN observation shows bar-like extended structure around the pulsar. The symmetric structure, if interpreted as pulsar equatorial outflow, indicates the pulsar spin vector. Ng & Romani (2007, in preparation) apply pulsar wind torus fitting to measure the PA of the symmetry axis. The pulsar birth site may be inferred from the radio image (Fig. 3 in Wang et al. 2001), where the peak of the PWN radio emission is at  $\alpha = 05^{\text{h}}37^{\text{m}}44^{\text{s}}.5(5)$ ,  $\delta = -69^{\circ}10'11''(2)$  (J2000). Then, adopting the kinematic age of 5 kyr (Wang & Gotthelf 1998), the pulsar velocity is  $630 \text{ km s}^{-1}$ . While the initial spin period is unknown, with its current  $P = 16 \text{ ms}$  we can safely assume the pulsar had a  $P_0$  range of

8 – 16 ms.

*PSR J1833–1034* Camilo et al. (2006) suggest a young kinematic age  $\lesssim 1000$  yr for the pulsar, which implies an initial spin period of  $P_0 \gtrsim 55$  ms. They also estimate the PA of the pulsar spin axis from the ellipticity of the PWN. Ng & Romani (2007, in preparation) fitted a model torus to the X-ray data and obtained similar results. Following Camilo et al. (2006), we found the geometrical center of G21.5–0.9 at  $\alpha = 18^{\text{h}}33^{\text{m}}33^{\text{s}}.4(3)$ ,  $\delta = -10^{\circ}34'12''(3)$  (J2000). If this is the explosion site, the offset from the pulsar position gives an estimated velocity of  $125 \text{ km s}^{-1}$ .

*PSR J0205+6449* The *CXO* images of this pulsar in 3C58 have been noted as having a prominent central torus and polar jets, and fitting of these provides a robust spin position angle (Ng & Romani 2007, in preparation). The position of the pulsar birth may be inferred from the SNR radio expansion center to be at  $\alpha = 02^{\text{h}}05^{\text{m}}31^{\text{s}}.32(3)$ ,  $\delta = +64^{\circ}49'58''.7(5)$  (J2000) (M. F. Bietenholz, private communication). Recently Gotthelf, Helfand, & Newburgh (2007) have identified a thermal X-ray shell in 3C58 with a similar center. If one assumes that 3C58 is the remnant of SN 1181, one gets an initial pulsar spin of 60 ms (Murray et al. 2002) and a rather large velocity of  $\sim 840 \text{ km s}^{-1}$ . The X-ray and radio evidence, however, suggest an older age of 3000–5000 yr. This would imply a shorter initial  $P_0$  and a transverse velocity of  $\sim 140 - 230 \text{ km s}^{-1}$ . While we plot values for the commonly assumed 825 yr age, these values and the pulsar’s status as a ‘3-D object’ are certainly open to question. A pulsar proper motion would resolve these difficulties.

*PSR B1706–44* A clear equatorial torus and polar jets were found in *CXO* data by Romani et al. (2005), where a robust spin position angle and inclination were fit. This pulsar is often associated with the SNR shell G343.1–2.3; comparing the total energy of the SNR and PWN, Romani et al. (2005) suggested  $P_0 = 60 - 80$  ms. Also, if born at the geometric center of the SNR shell, the pulsar velocity is  $\sim 650 \text{ km s}^{-1}$ . However, the PWN morphology and interstellar scintillation velocity limits make such a high speed questionable. Uneven SNR expansion could, for example, make the birth site much closer. Again, an interferometric pulsar proper motion would be particularly valuable.

*PSR B1800–21* Radio images spanning  $\sim 10$  years give an astrometric proper motion measurement of the pulsar with an accuracy of  $2.5 \text{ mas yr}^{-1}$  (Briskin et al. 2006). The Chandra X-ray observation shows symmetric PWN structure around the pulsar, which is fitted by Ng & Romani (2007, in preparation) to measure the spin orientation. However, no initial spin estimate is available for this pulsar.

*PSR J1124–5916* While the PWN image in the initial *CXO* HRC observation showed noticeable ellipticity (Hughes et al. 2003), this axis was not clear in a subsequent ACIS

exposure. A scheduled deep ACIS observation could help to resolve this structure. A PWN axis would be quite useful here as a robust proper motion axis and a reasonable age and  $P_0$  estimate are available from the highly symmetric parent SNR.

#### 4. SIMULATIONS

With our pulsar samples defined, we are now ready to constrain the kick models. We proceed by making Monte Carlo realizations of a given kick model, drawing pulsar spin and kick parameters and kick angles from the model distribution, simulating many pulsar realizations (by integrating according to the equations in §2.2) and projecting onto the sky plane to produce the observables for comparison with the pulsar sample. The comparison for a given set of true pulsars is made using a maximum likelihood estimate of the probability of getting that observed set from the Monte Carlo model.

Of course, any physical model will have a distribution of values for the kick parameters rather than single values. What we attempt to extract from our comparison with the observed pulsars are the characteristic values in these distributions. For the kick geometry, we assume no preferential directions in the kick position  $\alpha$  and the azimuth angle  $\phi$ , hence  $\cos \alpha$  and  $\phi$  are distributed uniformly between -1 to 1 and 0 to  $2\pi$  respectively. The off-axis angle  $\theta$  is, however, a more interesting parameter as it is potentially related to the kick mechanism. Assuming the kick follows a Gaussian distribution around the surface normal,  $\theta$  is characterized by the dispersion  $\sigma$  in the Gaussian. Many authors (e.g. Hobbs et al. 2005) fit the pulsar velocity distribution with a Maxwellian. We adopt this form for the momentum asymmetry  $\eta$ , with characteristic value  $\eta_0$ . We also attempted to use a simple Gaussian but this did not give a good distribution for the observed velocities; apparently, the larger Maxwellian tail is important for matching the observed sample. For the pre-kick angular velocity  $\Omega_i$ , we assume a Gaussian distribution with mean  $\bar{\Omega}$ . To minimize the fit parameters, we take the dispersion as  $\bar{\Omega}/3$ . The value used  $\Omega_i$  represents the angular frequency that the star with the same momentum will have after the proto-neutron star shrinks to its final radius. Our toy model approximates the time profile of the momentum kick as being proportional to the rapidly falling neutrino cooling light curve. A convenient way of introducing a characteristic kick time scale into the problem is by a delay to the ‘turn-on’ of the asymmetry, here parameterized as an exponential with a time constant  $\tau$ . This has the added advantage of approximating some reasonable physical scenarios for asymmetry growth. However, as the asymmetry occupies a smaller fraction of the momentum flux in the light curve tail, the effective  $\eta$  must grow. To avoid focus on this strong correlation, we thus report the equivalent asymmetry  $\bar{\eta}$  here, which corresponds to the same total thrust for

the case of  $\tau = 0$ , i.e.

$$\bar{\eta} \int L_\nu(t) dt = \eta_0 \int [1 - \exp(-t/\tau)] L_\nu(t) dt .$$

In brief, the kick model is characterized by the 4 ‘fitting parameters’:  $\eta_0$ ,  $\bar{\Omega}$ ,  $\tau$  and  $\sigma$ . The thrust is given by

$$F_\nu(t) = [1 - \exp(-t/\tau)] \eta L_\nu(t)/c$$

and the kick parameters are distributed as

$$\begin{aligned} \alpha, \phi &\sim \text{isotropic} \\ \frac{dN}{d\eta} &\propto \eta^2 \exp(-\eta^2/2\eta_0^2) \\ \frac{dN}{d\Omega_i} &\propto \exp\left[-\frac{(\Omega_i - \bar{\Omega})^2}{2(\bar{\Omega}/3)^2}\right] \\ \frac{dN}{d\theta} &\propto \sin \theta \exp(-\theta^2/2\sigma^2) . \end{aligned}$$

The factor  $\sin \theta$  above accounts for the area in polar coordinates. In the simulation, the approximation  $\sin \theta \approx \theta$  is taken to simplify the calculations. Also we tabulate the asymmetry results as  $\bar{\eta}$ , as noted above.

Given a set of fitting parameters, the kick velocity and spin vectors of  $N_{\text{sim}} = 2 \times 10^5$  pulsars are simulated. As the pulsar radial velocity is not an observable, the data samples are essentially only projected 2-D values on the sky plane. Therefore, the simulation results have to be projected before comparing to the observations. This is done by specifying 2 angles: the inclination angle  $\zeta$  of the spin axis to the sky plane, and the azimuth angle  $\phi_v$  of the velocity about the spin vector. While the latter is totally random,  $\zeta$  is sometimes actually known from pulsar wind torus fitting. In the simulation, each of the simulated vectors are projected  $N_{\text{proj}} = 50$  times, according to the measured  $\zeta$  (and its error) of an individual pulsar in the sample if this is known, or isotropically otherwise.

In order to compare the model prediction to measurements, we define a likelihood function similar to the typical  $\chi^2$  statistic

$$\mathcal{L}_\xi^{ij} \sim \exp \left[ -(\xi_{\text{obs}}^i - \xi_{\text{sim}}^j)^2 / 2(\sigma_\xi^i)^2 \right] .$$

For an observable  $\xi \in \{v, P_0, \vartheta_{\Omega \cdot v}\}$ ,  $\xi_{\text{obs}}^i$  is the  $i$ -th sample pulsar’s measurement with uncertainty  $\sigma_\xi^i$  and  $\xi_{\text{sim}}^j$  is the  $j$ -th simulation result. For the initial spin periods  $P_0$  and velocities based on the DM-estimated distance, uncertainties in the measurements are dominated by systematic errors which do not follow Gaussian properties. In this case, a boxcar function is used

$$\mathcal{L}_\xi^{ij} = \begin{cases} 1 & \text{if } |\xi_{\text{obs}}^i - \xi_{\text{sim}}^j| \leq \sigma_\xi^i \\ 0 & \text{otherwise} \end{cases} .$$

For each pulsar in the data sample, the likelihood function is then the product of all its observables, averaged over the simulations and projections

$$\mathcal{L}^i = \frac{1}{N} \sum_j \left( \prod_{\xi} \mathcal{L}_{\xi}^{ij} \right),$$

where  $N = N_{\text{sim}} \times N_{\text{proj}}$ . Finally, the total likelihood function is the product of all the pulsars in the data sample

$$\mathcal{L} = \prod_i^{N_{\text{obs}}} \mathcal{L}^i.$$

It is convenient to define a Figure-of-Merit (FoM) function for comparison between different models. As usual, it is defined as the negative log of the likelihood function  $\text{FoM} = -\log \mathcal{L}$ .

## 5. Results

Figures 5–7 show the projections of the likelihood function of our three kick scenarios for the main model parameters. Each panel shows four curves, with the minimum indicating the best-fit parameter values. The solid curve shows results obtained using all the objects in our pulsar sample; this generally has the tightest, best-defined minimum. However, as discussed in §3, some of the spin and velocity estimates for certain ‘3-D objects’ are quite model-dependent and can be questioned. We therefore also ran the FoM calculations with a ‘minimal’ set of ‘3-D pulsars’: the widely accepted Crab and Vela pulsars and PSR B0650–69, which is simple, but has large statistical error bars. The results are very similar to those for the full set, albeit with larger uncertainties. Finally, we ran fits with the ‘1-D’ and ‘2-D’ objects together and just the ‘1-D objects’ alone. Again, the fits are broadly consistent with the full set’s results, but as expected the minima are poorly constrained. Thus we confirm that our handful of well measured ‘3-D objects’ dramatically improve our knowledge of the birth kick properties, but apparently do not introduce major biases into the fits.

Our likelihood function is unnormalized. Since it is a product over individual objects, it is convenient to rescale the values for the curves computed for different sets of pulsars. This removes the gross scaling of FoM with number of objects and facilitates cross-comparison. In practice the results with different object sets are normalized by dividing all by the corresponding best-fit FoM values for the  $\nu$ -transport model for the same data set. Note that, with the exception of the ‘1D+2D’ (dashed line) fit to the static model, all minima occur at  $\text{FoM} > 1$ . Also the ‘ $\nu$ -transport’ model has narrower minima. This means that this model,

in addition to being the most physical, provides the best description of the full data set of the three scenarios tested.

It is useful to understand how the ‘1-D objects’ can provide some model constraints, i.e. how the pulsar velocity distribution is sensitive not only to the asymmetry  $\eta$ , but to the other kick parameters, as well. To illustrate, consider the case of large  $\sigma$  or small  $\bar{\Omega}$ , i.e. when kick-induced spin is important. When the pulsar is spun up, the induced linear and angular momenta are always orthogonal. In this case, the rotational averaging is efficient, generating many low velocity pulsars. In contrast, for large  $\bar{\Omega}$  or nearly normal kicks (i.e. small  $\sigma$ ), the initial spin sets the averaging axis, and the final velocity is principally determined by the kick location. For example, a polar kick results in a fast moving pulsar, while an equatorial kick is quickly averaged to give a low final speed. Thus, for fast initial spinners, the kick velocity distribution becomes relatively uniform, as our model assumes no preferential kick direction. This is unlike the observed velocity distribution.

Of course, when only velocity values are available, there is a large co-variance between the model parameters, leading to a broad minimum in the multi-dimensional (projected) FoM curve. In fact, it is the handful of ‘3-D objects’ that break these degeneracies and best localize the minima, as the FoM curves illustrate. Even then, there are significant correlations in the fit parameters, as illustrated by Fig. 8. The points show the loci of the minimum in two dimensional cuts through parameter space for the  $\nu$ -transport model. Similar results are obtained for the other models. To be conservative, we quote here the ‘projected’ multi-dimensional errors on all the model parameters. The single-parameter errors are, in general, significantly smaller. Table 2 reports the best-fit parameters for the models, with  $1\sigma$  confidence intervals estimated from the bootstrap percentiles (Efron & Tibshirani 1993). We generated  $10^5$  bootstrap samples and quote  $1\sigma$  errors from the standard normal 68% interval of the bootstrap replica distribution. The two dot sizes in Fig. 8 show the loci of the ‘ $1\sigma$ ’ and ‘ $2\sigma$ ’ minima.

There are some robust trends in the fitting results. All four of our basic model parameters are significantly constrained and, with the exception of  $\tau$  in the ‘static’ model, they have significantly non-zero values. Thus, we conclude that in all of our scenarios a finite pre-kick spin and a finite tangential component to the kick are required. In some sense, we consider the  $\nu$ -transport model to be the most physical. The best parameters for this model are closer to those of the static model than to the shrinking ‘quasi-stationary’ model. Thus, the kick is somewhat insensitive to the initial envelope shrinkage of the  $\nu$ -transport model. However, it should be noted that the  $\nu$ -transport model strongly prefers a finite  $\tau \sim 3\text{s}$ . This *ensures* that the kick is insensitive to the initial large envelope phase. Interestingly, if  $\tau$  is forced to be small for this model the best fit  $\bar{\eta}$ ,  $\sigma$  and  $\bar{\Omega}$  move much closer to the preferred

‘quasi-stationary’ values (Fig. 8). In this limit, the kick is dominated by the large-radius initial phase of the cooling curve.

The final angular velocity (after the proto-neutron star cooling and kick) has a very broad distribution, which peaks at  $\sim 120 \text{ rad s}^{-1}$  for the  $\nu$ -transport model. Similar results are obtained for the other models. With the pre-kick spin  $\Omega_i$  of only  $10\text{--}30 \text{ rad s}^{-1}$ , this indicates that most ( $> 90\%$ ) of the spin is induced by the kick, as suggested by Spruit & Phinney (1998). Unfortunately, so few initial spin estimates are available at present that the post-kick spin distribution cannot yet be compared with the data.

The distribution of final velocities for the best-fit  $\nu$ -transport model constrained by the full data sample is plotted in Fig. 9. The observed velocities represent reasonable draws from that model, with a K-S probability of 0.3, although the model predicts some additional low velocity pulsars. Similarly, Fig. 10 shows the model and data distributions of the alignment angles. The left panel compares the model angle distribution and the data. This is the alignment angle range that is actually used in the fits. The K-S statistic gives a moderately poor fit with a probability of only 0.08 that the data and model have the same distributions. Note, however that the ‘2-D pulsars’ with angles determined by polarization have, by fiat,  $\vartheta < 45^\circ$ . In the right panel we fold the model curve back to  $\vartheta < 45^\circ$ . The data match this distribution very well, with the K-S probability increased to 0.98. If our model is correct, about 20% of the ‘2-D’  $\vartheta$  values should be  $> 45^\circ$ . Note also that a few of the ‘3-D’ measurements have large errors and values  $> 45^\circ$  are allowed. We have tested this by randomly drawing  $\sim 3$  of the ‘2-D pulsars’, flipping the table values to  $\vartheta = 90^\circ - \vartheta$ , and re-fitting. The majority of the draws produce, as expected, best-fit parameters close to our adopted values, but deeper and tighter minima.

## 6. Discussion

We have explored the effect of an idealized model of a pulsar kick: a single finite duration thrust applied at a random but fixed point on the surface of a rotating, cooling proto-neutron star. This is a reasonable direct description of a class of models where neutrino anisotropy is imposed by a structure (e.g. magnetic) locked in the underlying neutron star. It is also a reasonable stand-in for other physical models where e.g. convection is controlled by a hot spot on the star surface. We note that our modeled momentum thrust can be considered as the net anisotropy of any number of kicks, as long as the anisotropy maintains a fixed pattern and follows the evolving core luminosity. Our models do not directly address the effects of multiple, completely random thrusts, but as first described by Spruit & Phinney (1998) and as confirmed in recent model integrations of Wang et al. (2006b), multiple kicks

tend to wash out any anisotropy; the net effect of a large number of kicks is to produce little or no correlation between motion and spin, contrary to recent observations. Our simulations also do not directly test the gravity-driven kicks described by Scheck et al. (2006) since for a rotating star these are almost certainly directed at the pole. Their scenario also does not include the kick-induced spin and rotational averaging described here. The technique described here for confronting parameterized models with the pulsar data set can, and should, be applied to formulations that probe such kick physics. However, we expect that the basic parameter estimates here, describing kick direction timescale and magnitude, can be a useful guide for evaluating a wide range of models.

While our model is certainly a simplified parameterization of real physics, it does produce some surprisingly complex behavior that can be discerned in the real pulsar data. The most interesting effects are only visible in the ‘3-D pulsars’, objects for which we have multiple observables and can measure their correlation within the population. Consider, for example, the projected angle  $\vartheta_{\Omega,v}$  vs. the post-kick initial pulsar spin frequency  $\Omega_0$  (Fig. 11). The model distribution shows that at intermediate initial spin periods 40 – 60 ms, we expect a substantial fraction of pulsars to be misaligned, with  $\vartheta_{\Omega,v} > 45^\circ$ . This is because during the kick, the spin was slow enough that the initial impulse induced the bulk of the spin, at orthogonal angles. In contrast, short spin period pulsars ( $P_0 < 20$  ms,  $\Omega_0 > 200$  rad s $^{-1}$ ) tend toward alignment due to spin averaging, and very long period pulsars ( $P_0 > 100$  ms,  $\Omega_0 < 60$  rad s $^{-1}$ ) are also aligned. The latter effect is ‘survivorship’; to retain a slow spin even with a decent kick the pulsar must have started as a slow spinner *and* have been kicked nearly radially. Similar correlations exist with the pulsar velocity, e.g. the fastest moving pulsars are expected to be slow spinners (Fig. 12): if the initial kick produces a large spin, then continued thrust ‘averages away’ and the pulsar never reaches high speeds.

While considering the 2-D correlations, it is interesting to look at the alignment-velocity correlation (Fig. 13). Here we may include many of the RV-model pulsars. It is not clear that these objects follow the expected correlations. First, there appears a dearth of misaligned pulsars at slow speeds. However, two effects may explain this. First, truly slow movers are selected against in the data sample as they are unlikely to have either a significant astrometric or timing proper motion. Second, we should remember that all RV pulsars have been *forced* to have  $\vartheta_{\Omega,v} < 45^\circ$ . It is possible that at least a few of the slower pulsars are in fact orthogonal. What about the pulsars at large space velocity in this plot? Well, the model suggests that these should show good alignment. Two of the ‘3-D pulsars’ PSRs B1706–44 and J0205+6449 in 3C58 show surprisingly large  $\vartheta_{\Omega,v}$  for their speed. However, note that the speed plotted for PSR J0205+6449 assumes a birth date of CE 1181. If, as appears increasingly likely (Gotthelf, Helfand, & Newburgh 2007), the pulsar is actually  $\geq 3,000$  years old, then the object falls near the peak of the expected distribution. Similarly, the



large velocity inferred for PSR B1706–44 depends on travel from the present remnant center. Scintillation measurements suggest a much slower speed, requiring an asymmetric SNR or even non-association; these again put the pulsar near the peak of the model distribution. Further note the large error bar on the alignment angle of PSR J1833–1034 in G21.5–0.9. This is set by the uncertainty in the SNR expansion center position. It would not be very surprising if this object, as well as the neutron star CXOU J061705.3+222127 in IC 443, would appear at  $\vartheta_{\Omega.v} > 45^\circ$ .

Recall that for the 2-D polarization objects, set to  $\vartheta_{\Omega.v} < 45^\circ$  by fiat, we might expect that 3-4 are actually at large  $\vartheta$ , emitting in the opposite polarization mode. This would not, of course, significantly dilute the general trend noted by e.g. Johnston et al. (2005). that RV model fits correlate with proper motion vectors. It is not clear if we will be able to understand the radio emission well enough to remove this  $\pi/2$  ambiguity. Happily the direct X-ray PWN fits do not suffer this problem, so more such measurements should expose a few poorly aligned objects. Globally, we expect fast pulsars to be well aligned. Slow pulsars will have a significant fraction of poorly aligned objects. Note that additional velocity components, e.g. orbital velocity for pulsars released from binaries, will enhance this trend.

Are there any serious challenges to our proposed model? Well, yes. PSR B1508+55 is fast and has a relatively large  $\vartheta_{\Omega.v} = 23^\circ \pm 7^\circ$ . This is very difficult to produce with the sort of kick scenarios that we describe. We would predict that improved spin measurements would prefer smaller  $\vartheta < 15^\circ$ . If a large misalignment perseveres, some amendment is needed to the kick scenario.

What about the substantial velocities which may arise naturally due to convection, when  $m = 1$  modes dominate (Scheck et al. 2006)? These kicks make *vector* predictions differing from those modeled here. For example, these authors suggest that fast spinners produce strong  $m = 1$  modes and thus only these attain high space velocities (opposite to the pattern of Fig. 12). Also, they suggest that slow spinners ( $\lesssim 60 \text{ rad s}^{-1}$ ) should be poorly aligned (cf. Fig. 11). This picture may also produce a bi-modal distribution of pulsar speeds; it is presently unclear if such bi-modality exists, but this would be an important test of the model. Perhaps the most interesting *vector* test of this down-flow kick scenario should come from binary pulsars, where a rotation-controlled  $m = 1$  mode predicts a kick along the binary orbit normal. We have not discussed binary kicks in this paper, deferring to a future publication.

Also, we should at least comment on the physical plausibility of our fit values. The effective asymmetry  $\bar{\eta}$  is quite large. If this were strictly induced at the neutrino photosphere, this would represent a large asymmetry. In the simple magnetic field picture this requires very large (although possibly transient) fields of  $\sim 10^{15.5-16} \text{ G}$ . Thus, a momentum asymmetry

mediated by coupling to matter would be quite appealing, as the field requirements are lower. The pre-kick spin periods are, as noted above, generally quite low. This argues for effective core-envelope coupling, possibly magnetic, in the pre-collapse progenitor (Spruit & Phinney 1998). What about the modest  $\sigma \approx 0.2 - 0.4 \approx 10^\circ - 20^\circ$  angle of the kick to the normal? This does seem quite natural in a magnetically-induced asymmetry model, where a dipole centered at  $\sim R_{NS}\sigma/2$  would cause such an angle. Pictures where the kick is due to matter fall-back, would tend to accrete matter with a large specific angular momentum. While effective at re-spinning the star, this would tend to have a large  $\sigma > 1$  and would, of course, suggest a strong trend to  $\vartheta_{\Omega,v} \sim 90^\circ$ , which are not observed.

Finally, we come to the time delay in the kick asymmetry. Since the initial neutrino flux falls off exponentially, the delay  $\tau$  can be thought of as selecting a characteristic timescale for the momentum thrust. As already noted, this has a strong covariance with the kick amplitude and with the pre-kick spin  $\Omega_i$ , with small delays requiring smaller kicks and faster spins. For example the best-fit ‘static’ model is consistent with no delay and has  $\Omega_i \approx 10 - 15 \text{ rad s}^{-1}$ . The quasi-stationary model prefers a  $\sim 1 \text{ s}$  delay and has  $\Omega_i \approx 20 - 40 \text{ rad s}^{-1}$ . Interestingly all the fits to proper motion data alone prefer some substantial delay, implying that long kicks and significant rotational averaging are useful in producing the observed velocity distribution. Finally, the  $\nu$ -transport model very strongly excludes the no-delay solution. As noted above, this is required to avoid having the bulk of the momentum thrust while the star still has a large radius. What about a physical origin for this delay? In a picture where a large  $B$  field introduces the asymmetry, it is attractive to associate this field with early dynamo action in the proto-neutron star. Such dynamo theory is not well developed, but it is interesting that qualitative discussions (e.g. Thompson & Duncan 1993) suggest a characteristic time of  $\sim 1 - 3 \text{ s}$  for a convectively-driven dynamo to drive the field to saturation. If  $\eta$  grows as  $\sim 0.1B_{15}(MeV/\bar{E}_\nu)^2$ , then the kick gains in efficiency as the  $B$  field grows to its limit and as the neutrinosphere temperature drops. Thus, the preferred fit parameters, a delayed kick with modest tangential component and a slow-spinning pre-kick star, are quite consistent with our qualitative picture of a magnetic field induced asymmetry of a neutrino-driven kick. Only the large asymmetry fraction, implying a very large  $B$  field, stretches this scenario.

As usual, more observations will provide improved tests of this picture. In particular we would like to obtain more robust X-ray image measurement of pulsars with low space velocities. Improved polarization sweep position angles for a larger data set will help as well. However, the real key to progress is accurate measurements of proper motion vectors for more young pulsars, especially slow objects. This means that we need improved sensitivity to reach to higher distances and long baselines. High bandwidth VLBI studies extending over a decade are the key. To push to larger distances, we will also want improved distance estimates to allow the  $\vartheta$  measurements to be corrected for differential Galactic rotation. The

real challenge in collecting more ‘3-D pulsar’ measurements is the difficulty in estimating initial spin periods. While some estimates may be obtained from SNR and PWN modeling (e.g. van der Swaluw & Wu 2001), most will require either historical remnants or very regular shells with high precision expansion ages. There are not many such pulsars, and measuring braking indices and precise proper motion for these will not be easy. However, with improved X-ray measurements for robust orientations, improved radio measurements for polarization and motions, and improved population modeling, we can hope for a more refined exploitation of this new probe of neutron star birth dynamics.

This work was supported by NASA grant NAG5-13344 and by CXO grants G05-6058 and AR6-7003C issued by the Chandra X-ray Observatory Center, which is operated by the Smithsonian Astrophysical Observatory for and on behalf of the National Aeronautics Space Administration under contract NAS8-03060.

## REFERENCES

- Arras, P., & Lai, D. 1999a, *ApJ*, 519, 745
- Arras, P., & Lai, D. 1999b, *Phys. Rev. D*, 60, 043001
- Aschenbach, B., Egger, R., & Trümper, J. 1995, *Nature*, 373, 587
- Blaauw, A. 1961, *Bull. Astron. Inst. Netherlands*, 15, 265
- Blondin, J. M., & Mezzacappa, A. 2006, *ApJ*, 642, 401
- Brisken, W. F., Benson, J. M., Goss, W. M., & Thorsett, S. E. 2002, *ApJ*, 571, 906
- Brisken, W. F., Carrillo-Barragan, M., Kurtz, S., & Finley, J. P. 2006, *ApJ*, 652, 554
- Burrows, A., Klein, D., & Gandhi, R. 1992, *Phys. Rev. D*, 45, 3361
- Camilo, F., Ransom, S. M., Gaensler, B. M., Slane, P. O., Lorimer, D. R., Reynolds, J., Manchester, R. N., & Murray, S. S. 2006, *ApJ*, 637, 456
- Chatterjee, S. et al. 2005, *ApJ*, 630, L61
- Cordes, J. M., Romani, R. W., & Lundgren, S. C. 1993, *Nature*, 362, 133
- Deshpande, A. A., Ramachandran, R., & Radhakrishnan, V. 1999, *A&A*, 351, 195
- Dewey, R. J., & Cordes, J. M. 1987, *ApJ*, 321, 780

- Dodson, R., Legge, D., Reynolds, J. E., & McCulloch, P. M. 2003, *ApJ*, 596, 1137
- Efron, B., & Tibshirani, R. J. 1993, *An Introduction to the Bootstrap* (New York: Chapman and Hall)
- Faucher-Giguère, C.-A., & Kaspi, V. M. 2006, *ApJ*, 643, 332
- Fryer, C., Burrows, A., & Benz, W. 1998, *ApJ*, 496, 333
- Fryer, C. L., & Kusenko, A. 2006, *ApJS*, 163, 335
- Gaensler, B. M., Chatterjee, S., Slane, P. O., van der Swaluw, E., Camilo, F., & Hughes, J. P. 2006, *ApJ*, 648, 1037
- Gotthelf, E. V., Helfand, D. J., & Newburgh, L. 2007, *ApJ*, 654, 267
- Hester, J. J. 2000, *BAAS*, 32, 1542
- Hobbs, G., Lorimer, D. R., Lyne, A. G., & Kramer, M. 2005 *MNRAS*, 360, 974
- Hobbs G., Lyne A. G., Kramer M., Martin, C. E., & Jordan, C. A. 2004, *MNRAS*, 353, 1311
- Hughes, J. P., Slane, P. O., Park, S., Roming, P. W. A., & Burrows, D. N. 2003, *ApJ*, 591, L139
- Janka, H.-Th., Buras, R., Kifonidis, K., Plewa, T., & Rampp, M. 2003, in *Proc. of the ESO/MPA/MPE Workshop, From Twilight to Highlight: The Physics of Supernovae*, ed. W. Hillebrandt & B. Leibundgut (Berlin: Springer), 39
- Janka, H.-Th., Buras, R., Kifonidis, K., Rampp, M., & Plewa, T. 2004, in *Stellar Collapse*, ed. C. L. Fryer (Dordrecht: Kluwer), 66
- Janka, H.-Th., Scheck, L., Kifonidis, K., Müller, E., & Plewa, T. 2005, in *ASP Conf. Ser. 332, The Fate of the Most Massive Stars*, ed. R. Humphreys & K. Stanek (San Francisco: ASP), 372
- Johnston, S., Hobbs, G., Vigeland, S., Kramer, M., Weisberg, J. M., & Lyne, A. G. 2005 *MNRAS*, 364, 1397
- Kotake, K., Sato, K., & Takahashi, K. 2006, *Rep. Prog. Phys.* 69, 971
- Kramer, M., Lyne, A. G., Hobbs, G., Löhmer, O., Carr, P., Jordan, C., & Wolszczan, A. 2003, *ApJ*, 593, L31
- Lai, D., Chernoff, D. F., & Cordes, J. M. 2001, *ApJ*, 549, 1111

- Lyne, A. G., Pritchard, R. S., Graham-Smith, F., & Camilo, F. 1996, *Nature*, 381, 497
- Manchester, R. N., & Taylor, J. H. 1977, *Pulsars* (San Francisco: Freeman)
- Manchester, R. N., Mar, D. P., Lyne, A. G., Kaspi, V. M., & Johnston, S. 1993, *ApJ*, 403, L29
- Migliazzo, J. M., Gaensler, B. M., Backer, D. C., Stappers, B. W., van der Swaluw, E., & Strom, R. G. 2002, *ApJ*, 567, L141
- Murray, S. S., Slane, P. O., Seward, F. D., Ransom, S. M., & Gaensler, B. M. 2002, 568, 226
- Ng, C.-Y., & Romani, R. W. 2004, *ApJ*, 601, 479
- Ng, C.-Y., & Romani, R. W. 2006, *ApJ*, 644, 445
- Ng, C.-Y., Romani, R. W., Brisken, W. F., Chatterjee, S., & Kramer, M. 2006, *ApJ*, 654, 487
- Rampp, M., & Janka, H.-T. 2002, *A&A*, 396, 361
- Reynolds, S. P. 1985, *ApJ*, 291, 152
- Romani, R. W. 2005, in *ASP Conf. Ser. 328, Binary Radio Pulsars*, ed. F. A. Rasio & I. H. Stairs (San Francisco: ASP), 337
- Romani, R., W., & Ng, C.-Y. 2003, *ApJ*, 585, L41
- Romani, R. W., Ng, C.-Y., Dodson, R., & Brisken, W. 2005, *ApJ*, 631, 480
- Scheck, L., Kifonidis, K., Janka, H.-Th., & Müller, E. 2006, *A&A*, 457, 963
- Serafimovich, N. I., Shibarov, Yu. A., Lundqvist, P., & Sollerman, J. 2004, *A&A*, 425, 1041
- Socrates, A., Blaes, O., Hungerford, A., & Fryer, C. L. 2005, *ApJ*, 632, 531
- Spruit, H., & Phinney, E. S. 1998, *Nature*, 393, 139
- Tauris, T. M., & Takens, R. J. 1998, *A&A*, 330, 1047
- Thompson, C., & Duncan, R. C. 1993, *ApJ*, 408, 194
- van der Swaluw, E., & Wu, Y. 2001, *ApJ*, 555, L49
- Wang, Q. D., Gotthelf, E. V., Chu, Y.-H., & Dickel, J. R. 2001, *ApJ*, 559, 275

Wang, C., Lai, D., & Han, J. L. 2006a, *ApJ*, 639, 1007

Wang, C., Lai, D., & Han, J. L. 2006b, *ApJ*, in press

Wang, Q. D., & Gotthelf, E. V. 1998, *ApJ*, 494, 623

Zou, W. Z., Hobbs, G., Wang, N., Manchester, R. N., Wu, X. J., & Wang, H. X. 2005, *MNRAS*, 362, 1189

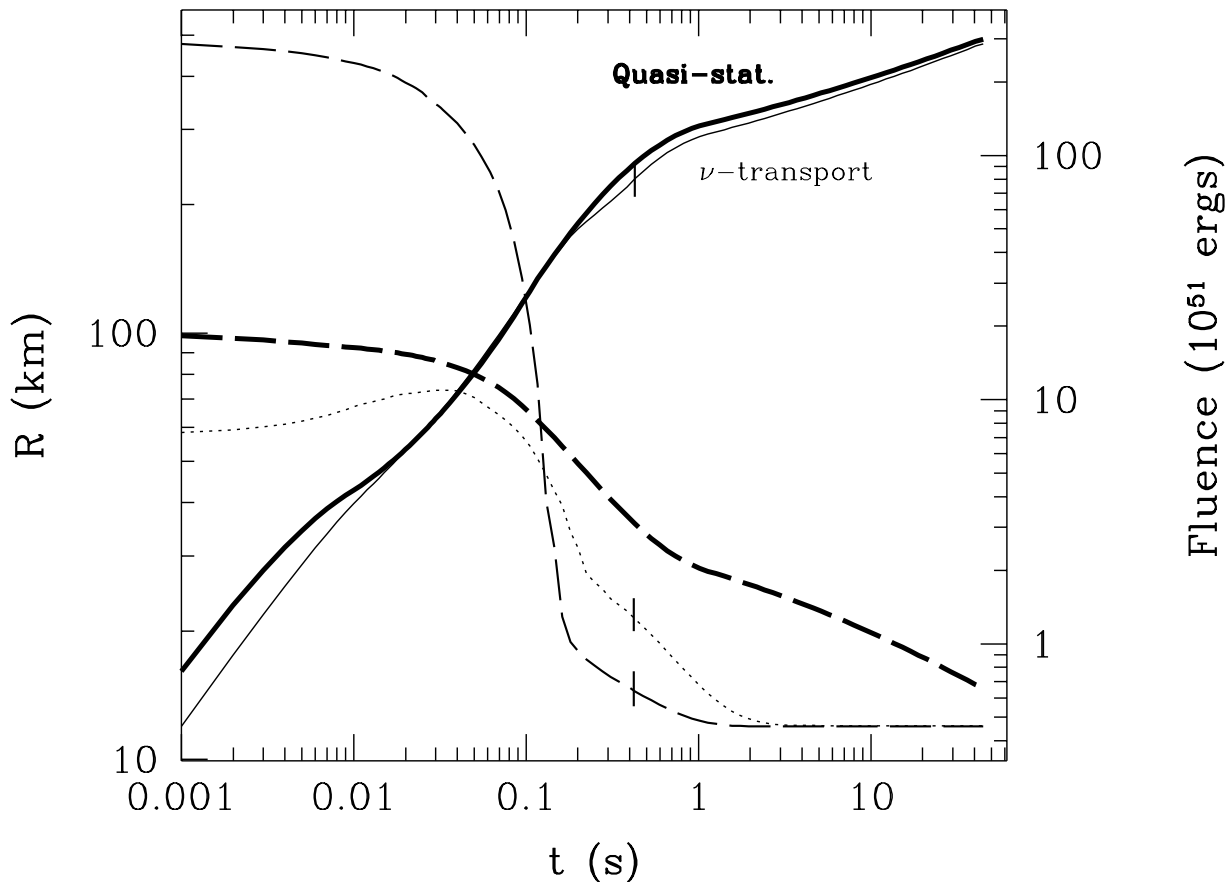


Fig. 1.— Proto-neutron star cooling. Evolution of the stellar radius and the neutrino fluence for the quasi-stationary model are shown in the thick solid and dashed lines respectively. The thin solid and dashed lines show equivalent values for the  $\nu$ -transport model (Janka et al. 2003), with the effective  $R$  of a uniform density sphere with the same instantaneous moment of inertia. The thin dotted line shows the radius of the neutrino-sphere in the  $\nu$ -transport model. The end points of the numerical simulation are marked; the curves are extrapolated to  $t = 50$  s.

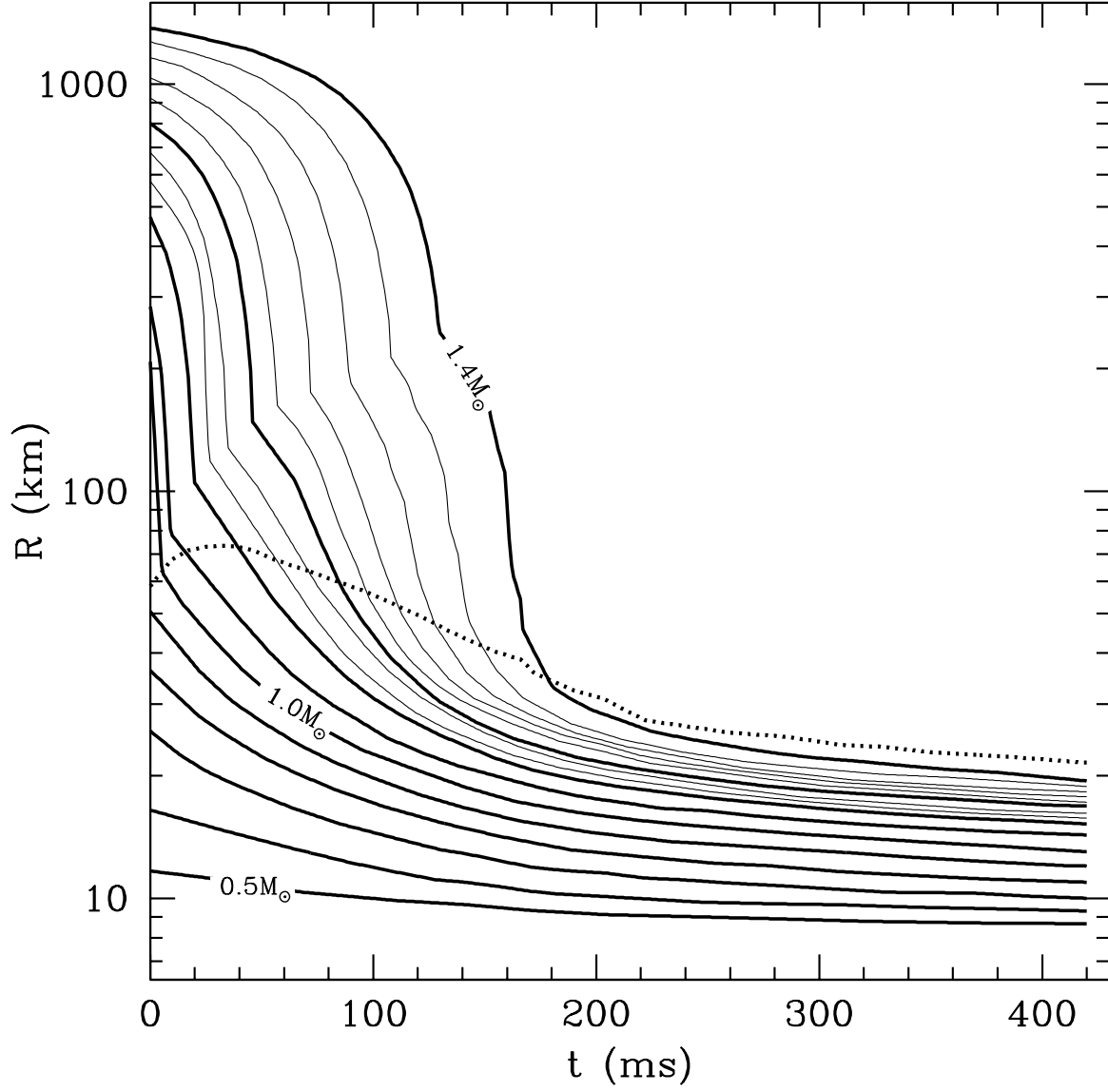


Fig. 2.— Mass shell trajectories of a proto-neutron star in the  $\nu$ -transport model, reproduced from Janka et al. (2003). Radius of the neutrinosphere is plotted by the dotted line.



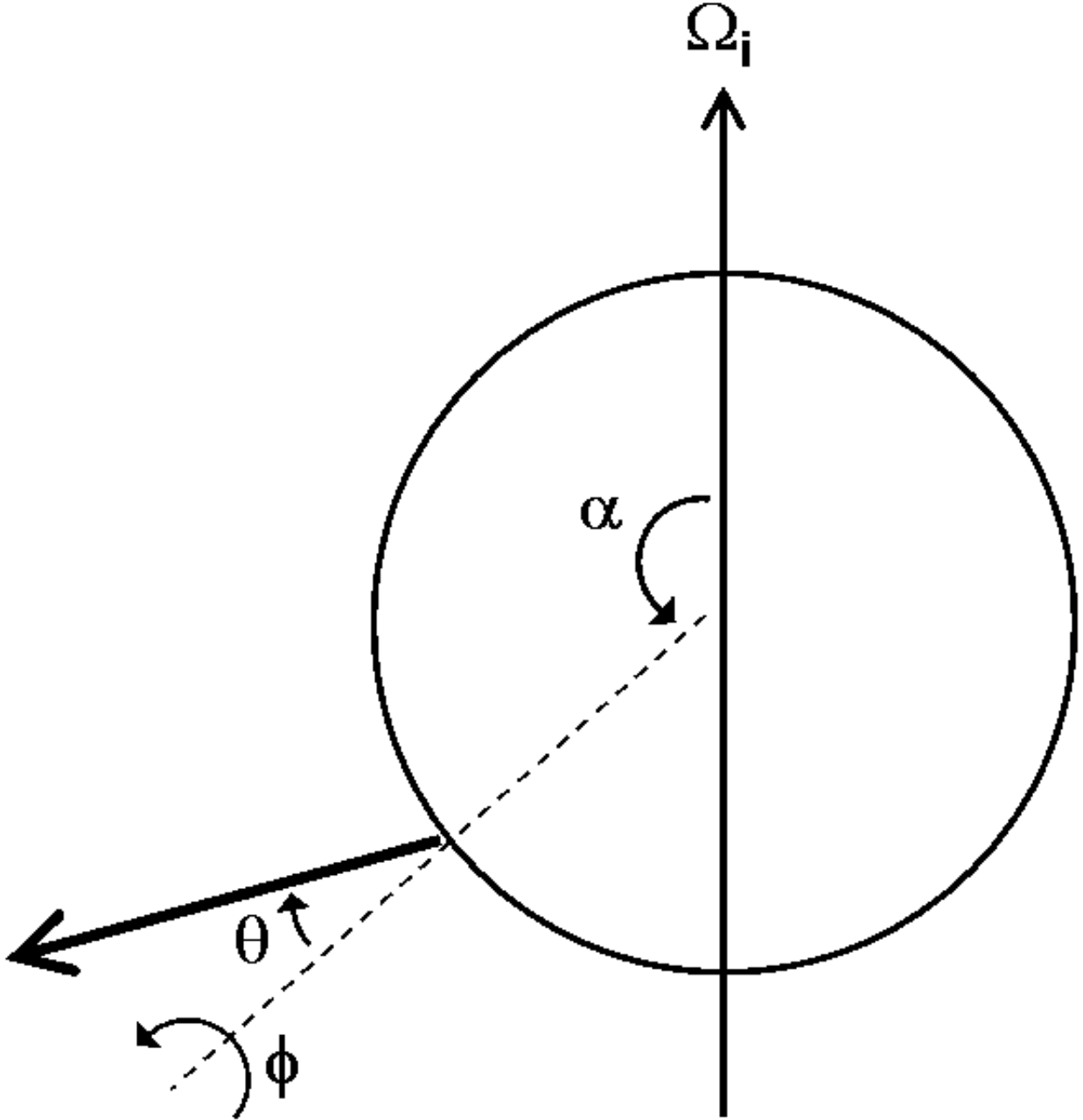


Fig. 3.— The kick geometric parameters:  $\alpha$  is the polar angle of the kick position,  $\theta$  is the off-axis angle of the kick from the surface normal,  $\phi$  is the azimuth angle of the kick about the normal,  $\Omega_i$  is the pre-kick angular velocity.

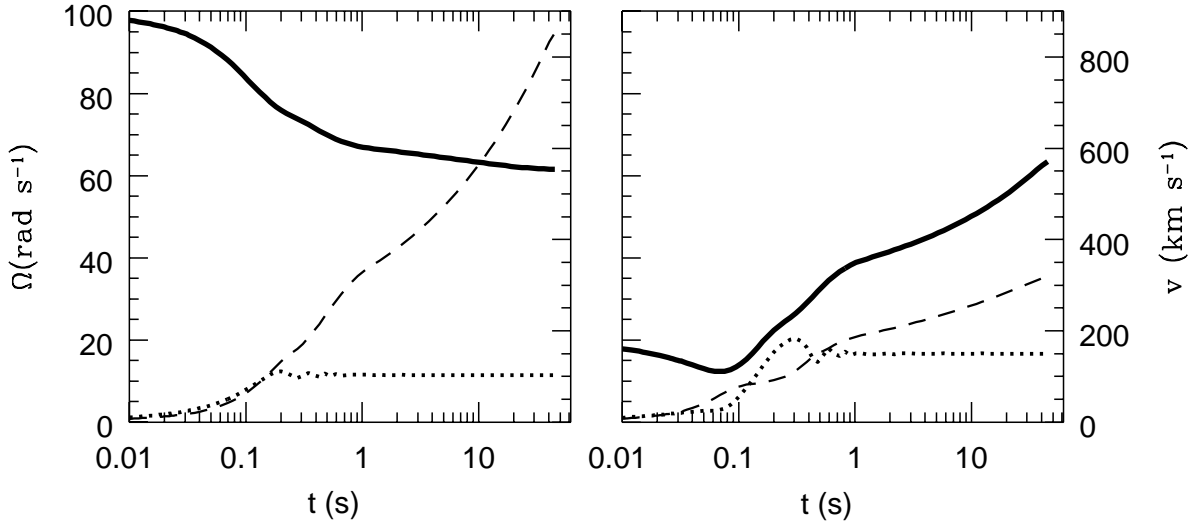


Fig. 4.— Two kick integrations with identical parameters ( $\alpha = \cos^{-1} 0.6$ ,  $\phi = 80^\circ$ ,  $\theta = 0.2$  rad), except  $\Omega_i = 100$  rad s $^{-1}$  (*Left panel*) and  $\Omega_i = 30$  rad s $^{-1}$  (*right panel*). The solid lines follow the instantaneous angular momentum, plotting the equivalent angular velocities with the moment of inertia at its final value. The dashed and dotted lines are the parallel and perpendicular components of the space velocity with respect to the instantaneous spin direction.

Quasi-stat Model

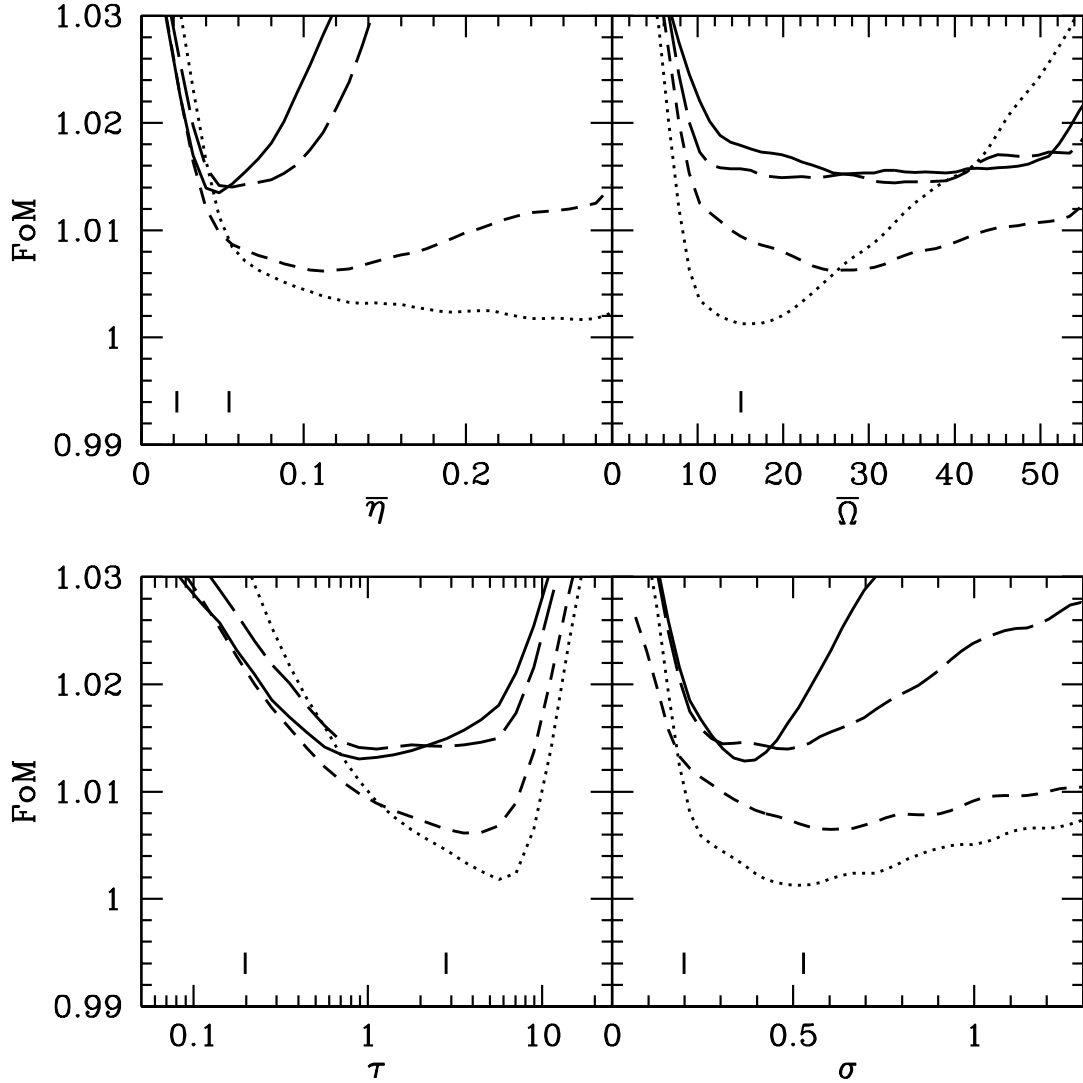


Fig. 5.— Projected FoM for individual parameters of the ‘quasi-stationary’ model. The solid lines show the full sample fit; the long dashed lines show the fit with the ‘1-D, 2-D pulsars’ and the ‘minimal set’ of ‘3-D objects’ (i.e. Crab, Vela and B0540–69); the short dashed lines show the fit with only ‘1-D’ and ‘2-D’ pulsars; the dotted lines show the fit with only ‘1-D pulsars’. Smoothing filters have been applied to the curves and the FoM scale has been normalized by the minimum ‘ $\nu$ -transport’ value for each data set. For the full sample curves, the upper and lower ‘ $1\sigma$ ’ intervals provided by the bootstrap analysis (Table 2) are indicated by the tickmarks. Comparison with the  $\Delta\text{FoM}$  at these confidence intervals and with Table 2 allows the reader to judge acceptable parameter ranges.

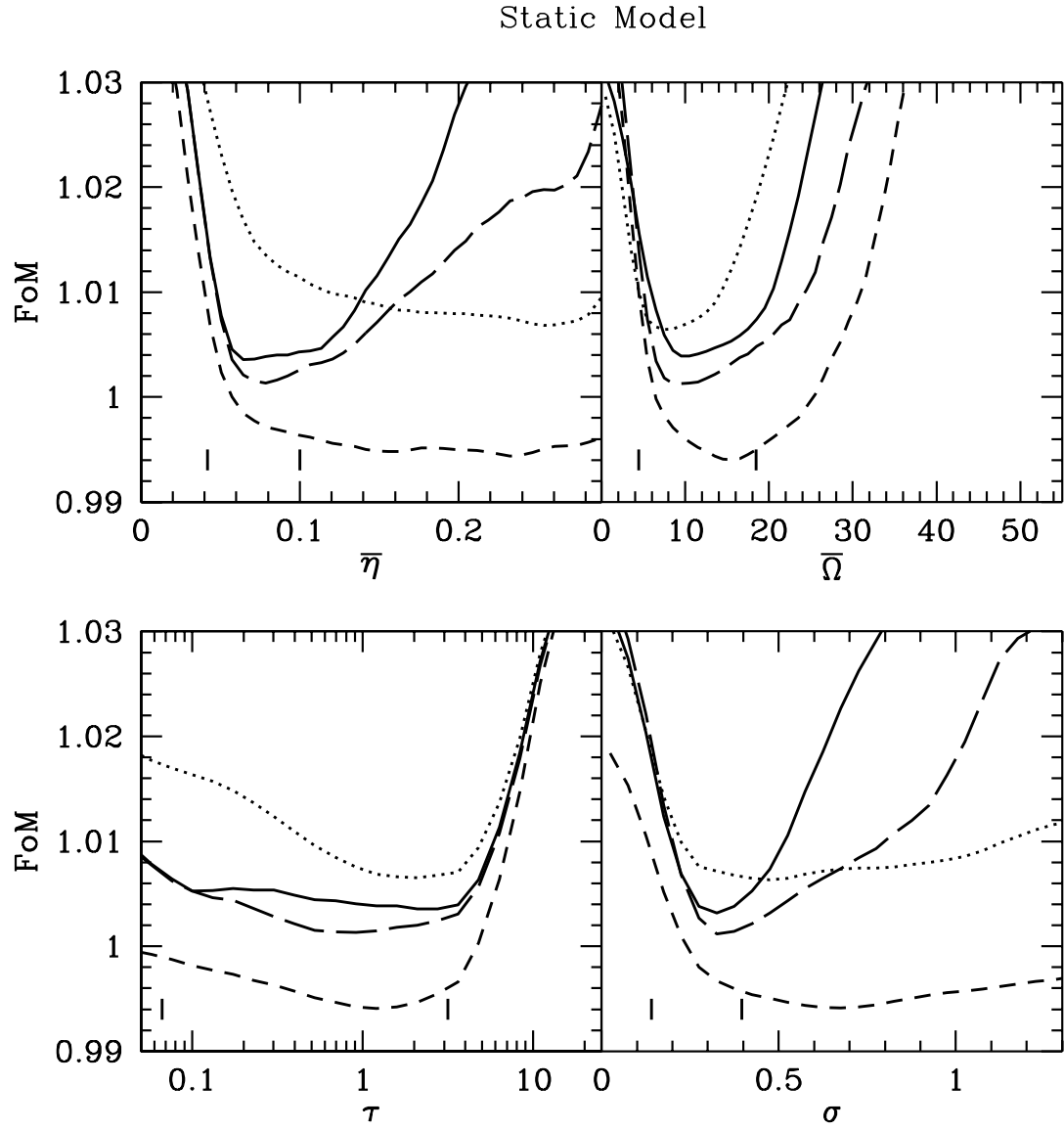


Fig. 6.— Same as Fig. 5, for the ‘static’ model.

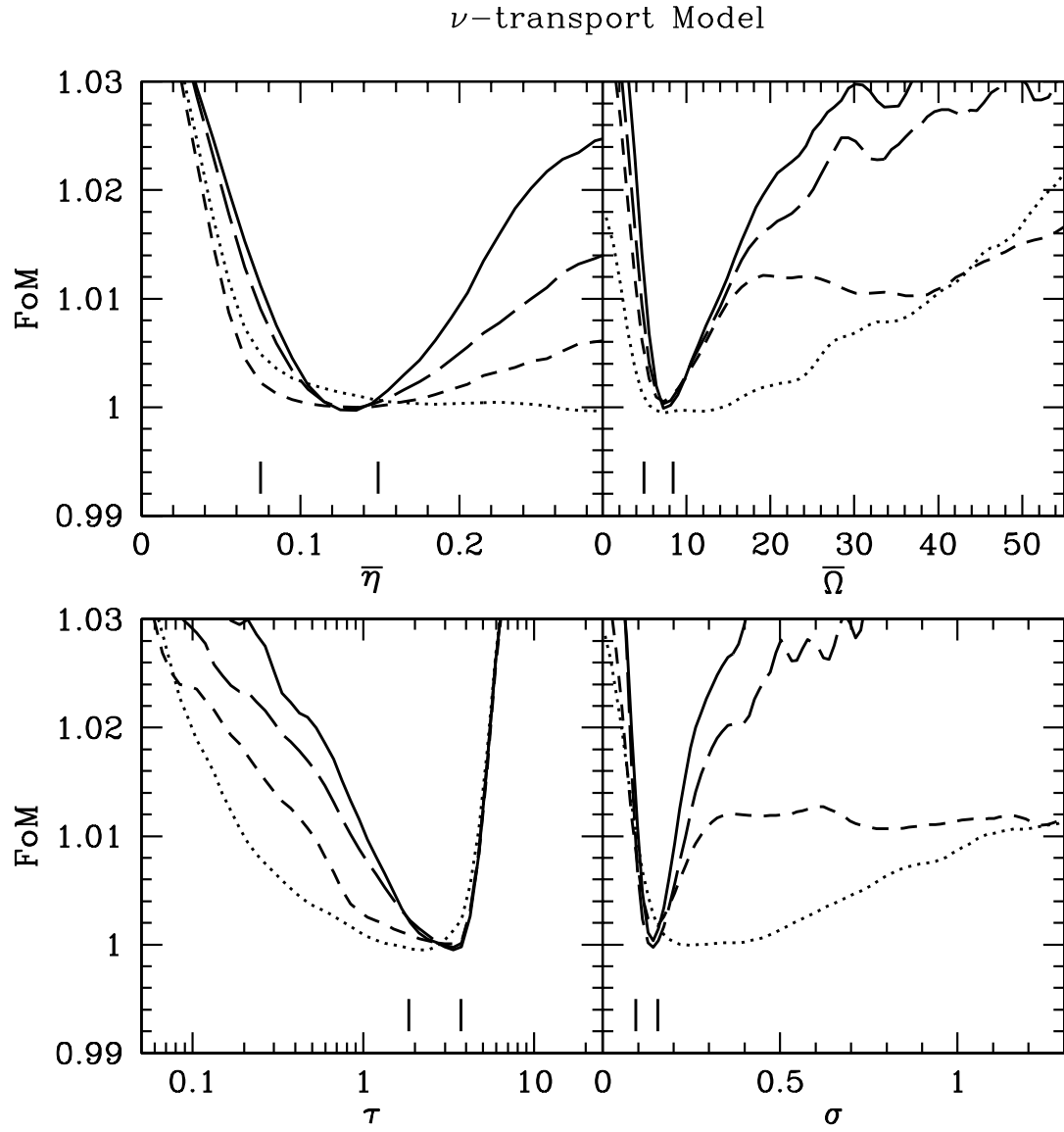


Fig. 7.— Same as Fig. 5, for the  $\nu$ -transport model.

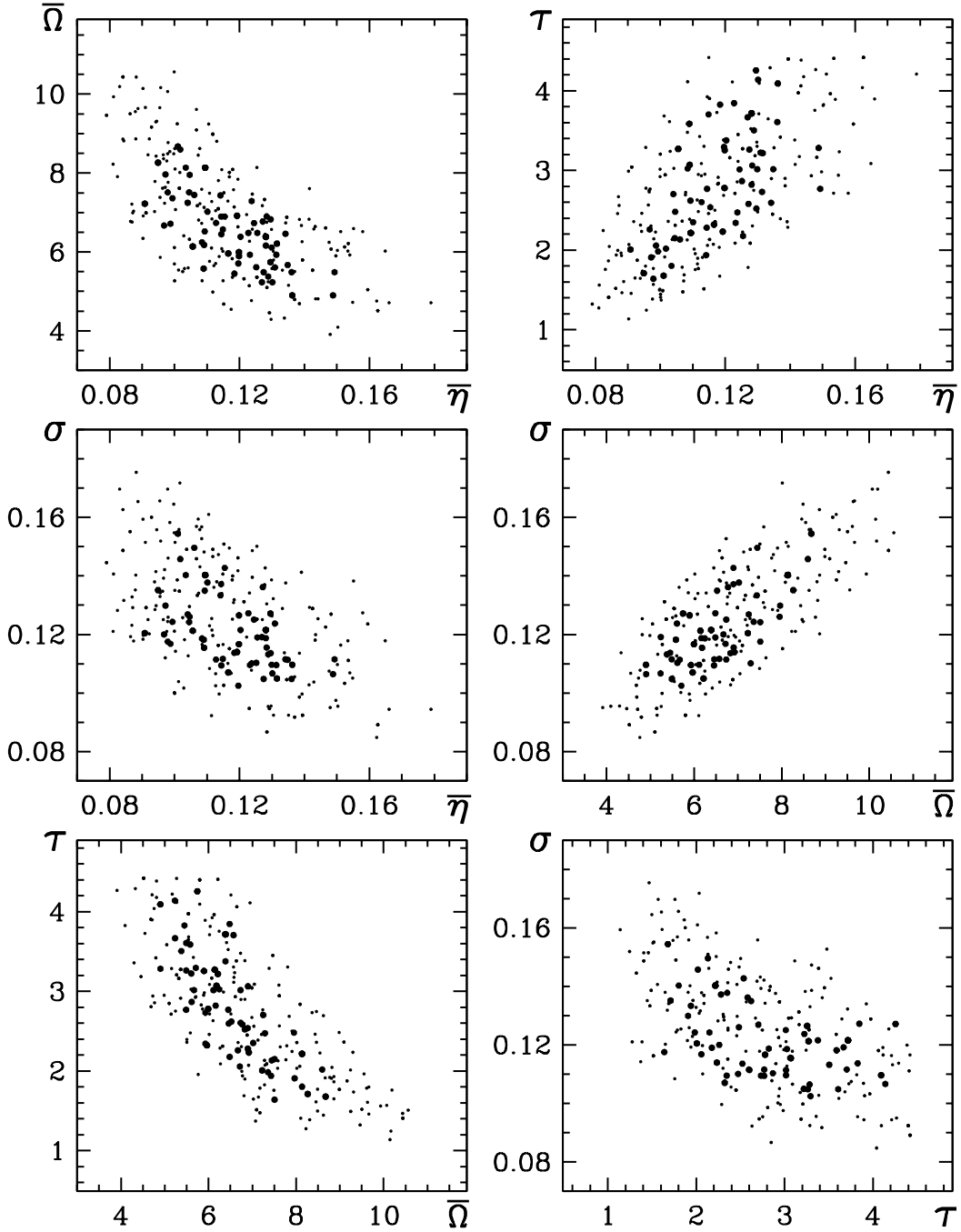


Fig. 8.— Correlations between fitting parameters for the best-fit  $\nu$ -transport model with full data sample. Large and small dots are simulations within 1 and  $2\sigma$  of the best fit FoM. Note that significant correlations remain between the parameters and that our full projected errors are (conservatively) larger than the single parameters uncertainties.

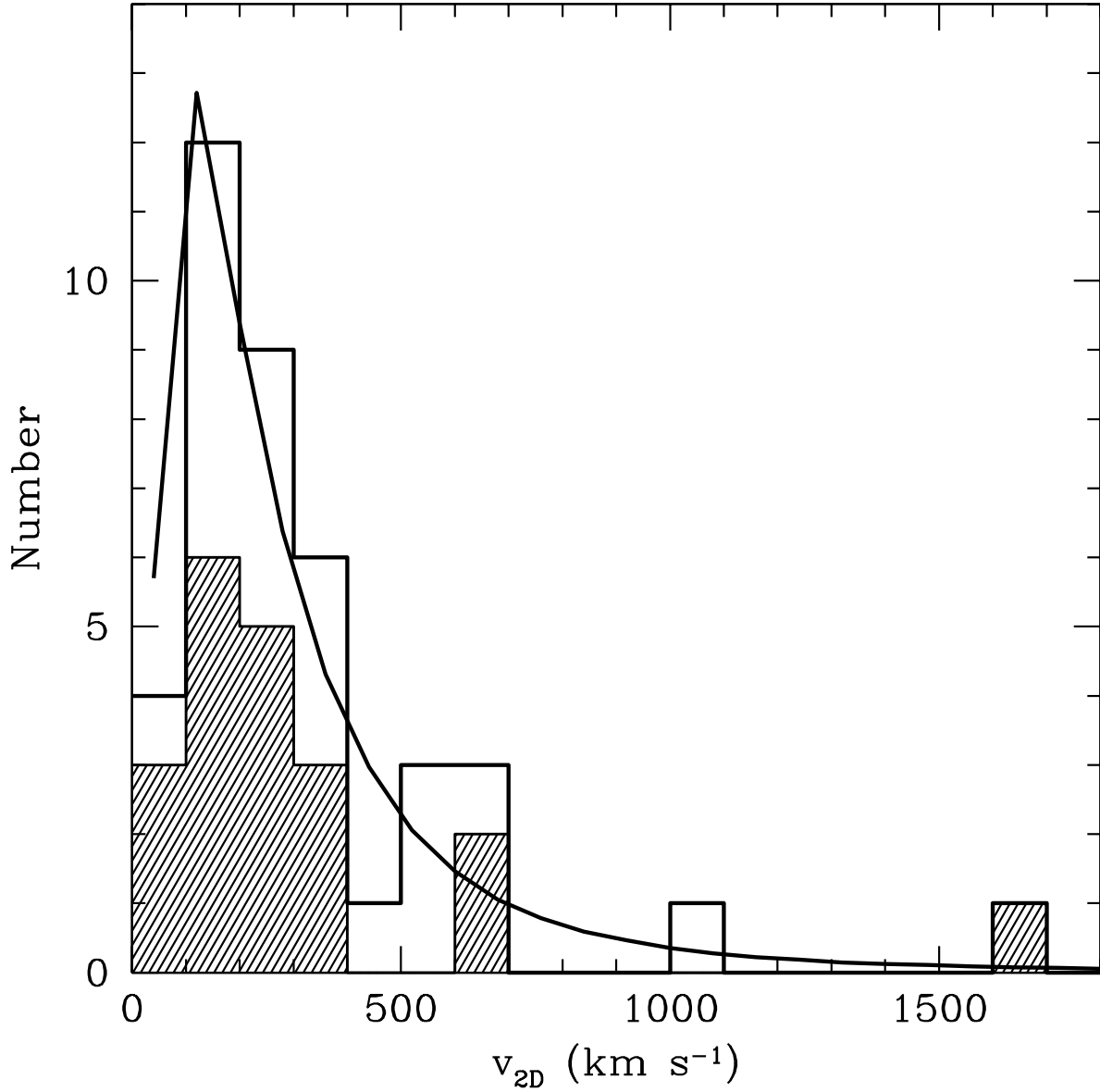


Fig. 9.— Velocity distributions of the best-fit  $\nu$ -transport model with the full data set, compared to the observed pulsars with proper motion measurements of  $> 2\sigma$  significance. The ‘1-D pulsars’ are shaded.

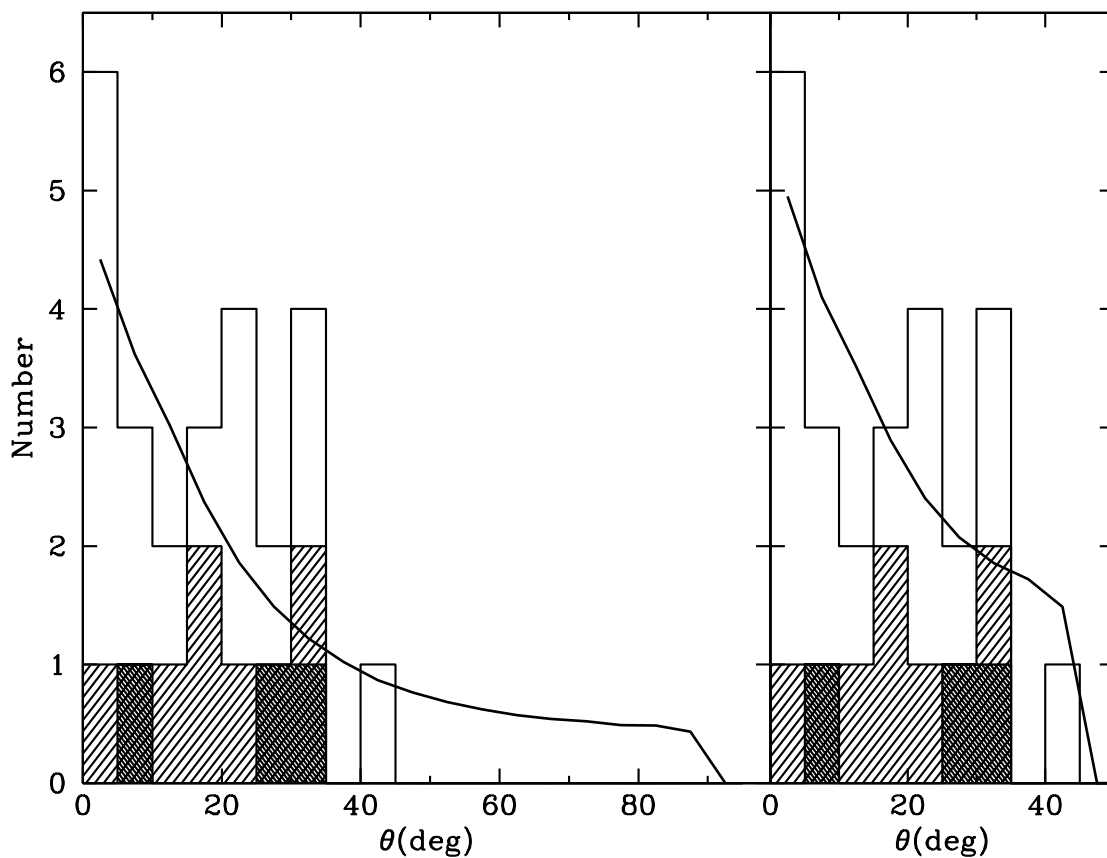


Fig. 10.— Alignment angles of the pulsar samples compared to the best-fit  $\nu$ -transport model with the full data set. The ‘3-D objects’ and the ‘minimal set’ are shaded in light and dark gray respectively. *Right panel:* Simulations are folded around  $45^\circ$  to illustrate the effects of the  $90^\circ$  ambiguity in alignment angles measured by radio polarization.



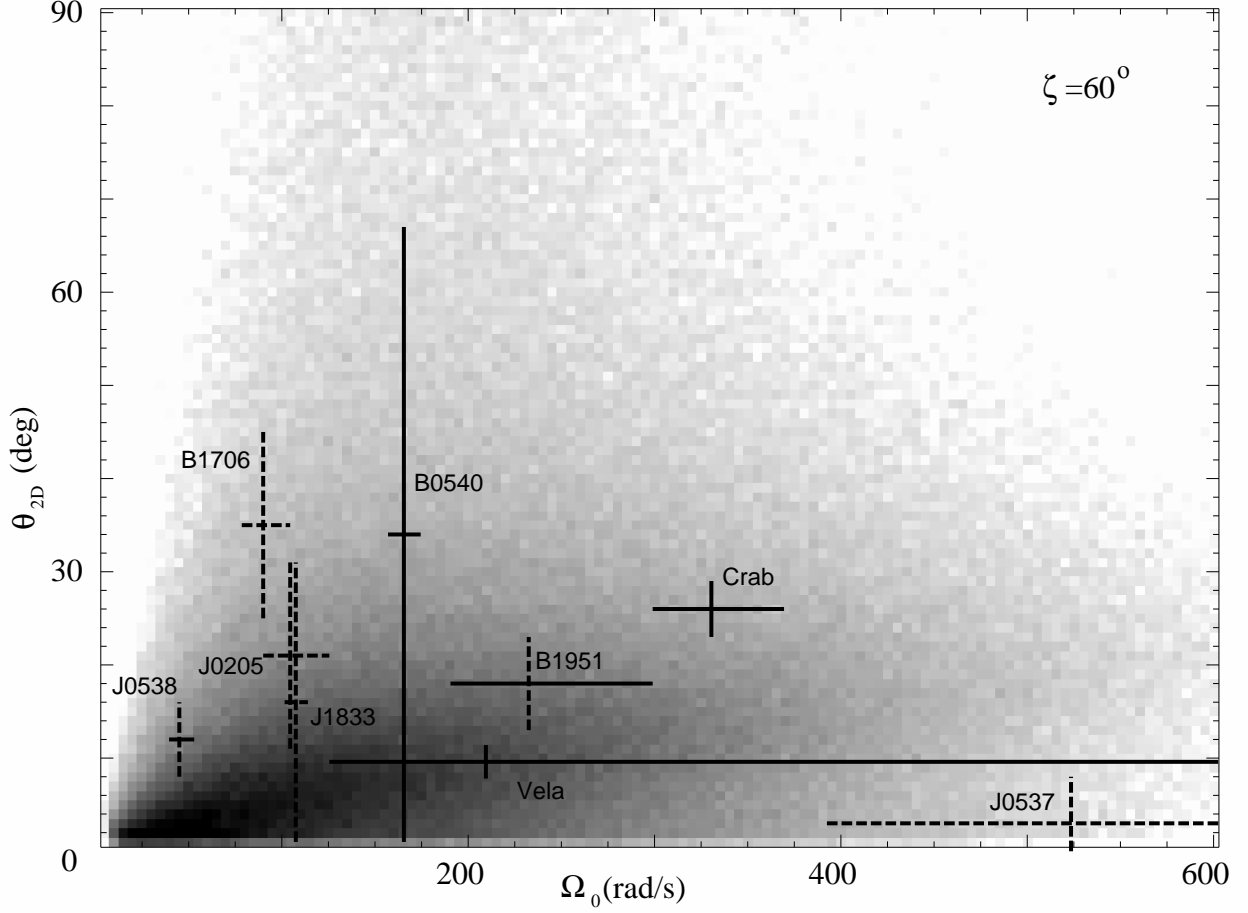


Fig. 11.— Distribution of alignment angle  $\vartheta_{\Omega,v}$  vs. post-kick initial spin  $\Omega_0$  for the best-fit  $\nu$ -transport model with the full data set. The simulations are projected for  $\zeta = 60^\circ$ , a typical value for the ‘3-D pulsars’. For these pulsars, measurements with model-dependent assumptions dominating the errors are shown by plotting the corresponding error flags in dotted lines.

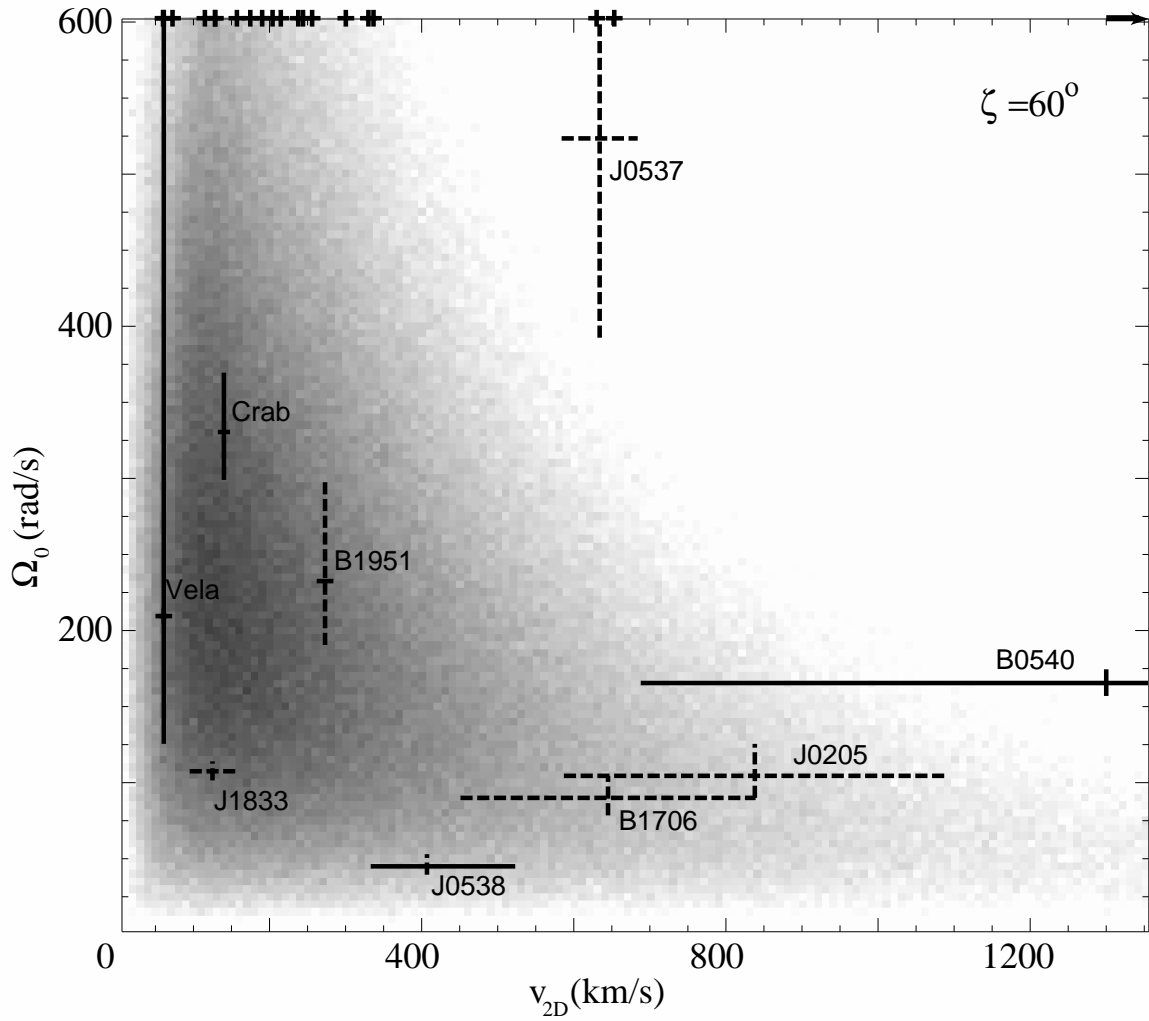


Fig. 12.— Distribution of pulsar post-kick initial spin vs. velocity for the best-fit  $\nu$ -transport model with the full data set. The simulations are projected for  $\zeta = 60^\circ$ . The velocities of the ‘1-D pulsars’ are marked at top. Again, systematic-dominated parameters of ‘3-D objects’ have dotted-line error bars.

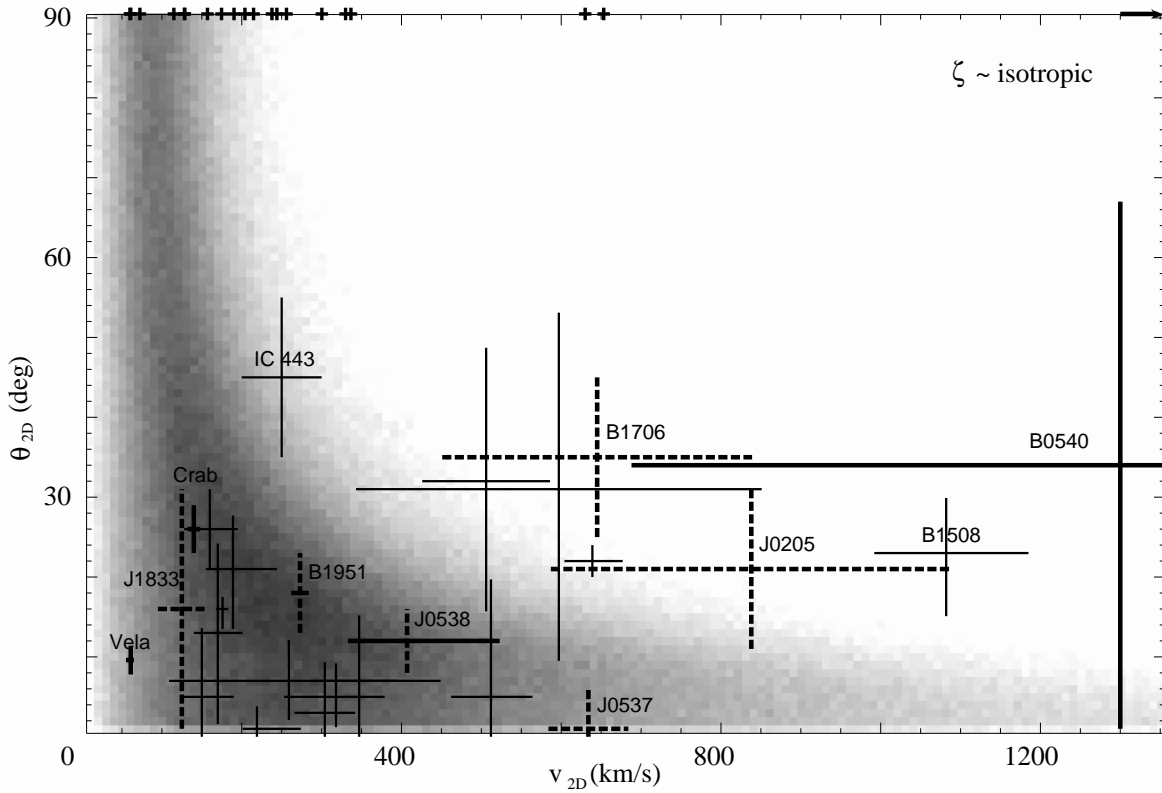


Fig. 13.— Distribution of alignment angle vs. kick velocity for the best-fit  $\nu$ -transport model with the full data set. Here we can plot many ‘2-D pulsars’, so the simulations are projected isotropically. The velocities of the ‘1-D pulsars’ are plotted on the top. ‘2-D objects’ are plotted by the thin lines. Measurements of ‘3-D objects’ have thick-lined error bars, with dotted lines for those parameters dominated by model-dependent systematics.

Table 1. Pulsar sample used in the analysis.

Pulsar	$v$ (km s <sup>-1</sup> )	$\Delta v^a$ (km s <sup>-1</sup> )	$\vartheta_{\Omega \cdot v}$ (°)	$P_0$ (ms)	$\zeta$ (°)	Ref.
1-D Pulsars						
B0114+58	190	±63	...	...	...	...
B0136+57	300	±68	...	...	...	...
B0355+54	61	+12/-9	...	...	...	...
B0402+61	653	±121	...	...	...	...
B0450+55	175	+20/-19	...	...	...	...
B0458+46	72	±33	...	...	...	...
B0540+23	215	±78	...	...	...	...
J0633+1746	128	±3	...	...	...	...
B0656+14	60	+7/-6	...	...	...	...
B0736-40	238	+200/-23	...	...	...	...
B0834+06	157	+20/-19	...	...	...	...
B1702-19	330	±152	...	...	...	1
B1749-28	630	±280	...	...	...	1
B1818-04	129	+21/-21	...	...	...	...
B1848+13	204	+25/-25	...	...	...	...
B2020+28	256	+114/-61	...	...	...	...
B2021+51	115	+18/-15	...	...	...	...
B2022+50	244	±33	...	...	...	...
B2217+47	337	±74	...	...	...	...
B2224+65	1605	+193/-188	...	...	...	...
2-D Pulsars						
B0628-28	318	+61/-64	5 ± 4	...	...	2
B0740-28	259	+190/-149	7 ± 5	...	...	2
B0823+26	189	+55/-34	21 ± 7	...	...	3
B0835-41	170	±30	13 ± 11	...	...	3
B0919+06	506	±80	32 ± 17	...	...	3
B1133+16	639	+38/-35	22 ± 2	...	...	2
B1325-43	597	±254	31 ± 22	...	...	3
B1426-66	150	+40/-24	5 ± 9	...	...	2
B1449-64	219	+55/-18	1 ± 3	...	...	2
B1508+55	1082	+103/-90	23 ± 7	...	...	3, 4
B1642-03	160	+34/-32	26 ± 5	...	...	2
B1800-21	347	+48/-57	7 ± 8	...	90 ± 2	6
B1842+14	512	+51/-50	5 ± 15	...	...	2
B1929+10	173	+4/-5	16 ± 2	...	...	2
B2045-16	304	+39/-38	3 ± 6	...	...	3
IC 443	250	±50	45 ± 10	...	...	5
3-D Pulsars						
J0205+6449	838	±251	21 ± 10	60 ± 10	91.0 ± 0.2	6
B0531+21	140	±8	26 ± 3	19 ± 2	61.3 ± 0.1	6
J0537-6910	634	±50	3 ± 5	12 ± 4	92.8 ± 0.8	6
J0538+2817	407	+116/-74	12 ± 4	139 ± 2 <sup>b</sup>	...	6
B0540-69	1300	±612	34 ± 33	38 ± 2	93.7 ± 5	6
B0833-45	61	±2	10 ± 2	30 ± 20	63.6 ± 0.1	6
B1706-44	645	±194	35 ± 10	70 ± 10	52 ± 2	6

Table 1—Continued

Pulsar	$v$ (km s $^{-1}$ )	$\Delta v^a$ (km s $^{-1}$ )	$\vartheta_{\Omega, v}$ ( $^\circ$ )	$P_0$ (ms)	$\zeta$ ( $^\circ$ )	Ref.
J1833-1034	125	$\pm 30$	$16 \pm 15$	$58 \pm 3$	$85.4 \pm 0.3$	6
B1951+32	273	$\pm 11$	$18 \pm 5$	$27 \pm 6$	$\sim 90 \pm 30$	6

<sup>a</sup>The errors in velocity are compiled from either the uncertainties in proper motion measurement, or distance estimates, whatever larger.

<sup>b</sup>An uncertainty of 20 ms is used in the calculation, as to represent a group of objects with slow spin.

References. — Unless specified otherwise, all pulsar velocities are from Hobbs et al. (2005) and references therein. (1) Zou et al. (2005); (2) Johnston et al. (2005); (3) Wang et al. (2006a); (4) Chatterjee et al. (2005); (5) Gaensler et al. (2006); (6) –see text.

Table 2. Best-fit parameters of the kick models. The best-fit values are obtained from the lightly smoothed curves in Fig. 5 – 7.

	$\bar{\eta}$	$\bar{\Omega}$	$\tau$	$\sigma$
Quasi-stat				
Full Sample	$0.05^{+0.01}_{-0.02}$	$26^{+37}_{-11}$	$0.9^{+1.9}_{-0.7}$	$0.39^{+0.14}_{-0.19}$
Minimal Set	$0.05^{+0.04}_{-0.03}$	$36^{+19}_{-23}$	$1.4^{+3.7}_{-1.0}$	$0.5^{+0.5}_{-0.2}$
1D+2D	$0.13^{+0.03}_{-0.10}$	$30^{+14}_{-10}$	$4^{+2}_{-3}$	$0.6^{+0.6}_{-0.17}$
1D	$0.24^{+0.03}_{-0.21}$	$13^{+9}_{-3}$	$5^{+3}_{-5}$	$0.5^{+0.6}_{-0.15}$
Static Model				
Full Sample	$0.07^{+0.03}_{-0.02}$	$9^{+10}_{-4}$	$1.0^{+2.1}_{-0.9}$	$0.32^{+0.07}_{-0.18}$
Minimal Set	$0.07^{+0.04}_{-0.03}$	$9^{+11}_{-3}$	$0.8^{+2.1}_{-0.73}$	$0.32^{+0.28}_{-0.14}$
1D+2D	$0.22^{+0.04}_{-0.12}$	$14^{+6}_{-3}$	$1.4^{+0.6}_{-1.2}$	$0.6^{+0.6}_{-0.17}$
1D	$0.26^{+0.20}_{-0.17}$	$7^{+3}_{-5}$	$2.3^{+1.9}_{-2.1}$	$0.4^{+0.5}_{-0.26}$
$\nu$ -transport				
Full Sample	$0.13^{+0.02}_{-0.06}$	$7^{+1}_{-3}$	$3.3^{+0.4}_{-1.5}$	$0.12^{+0.03}_{-0.03}$
Minimal Set	$0.13^{+0.04}_{-0.08}$	$8^{+20}_{-3}$	$3.3^{+0.5}_{-2.5}$	$0.14^{+0.23}_{-0.03}$
1D+2D	$0.13^{+0.10}_{-0.06}$	$7^{+27}_{-3}$	$3.5^{+0.2}_{-2.5}$	$0.13^{+1.2}_{-0.03}$
1D	$0.17^{+0.16}_{-0.05}$	$8^{+5}_{-5}$	$1.4^{+1.9}_{-0.5}$	$0.19^{+0.5}_{-0.05}$